

ARTICLE

Dia1 coordinates differentiation and cell sorting in a stratified epithelium

Robert M. Harmon^{1,2} , John Devany^{1,2,3} , and Margaret L. Gardel^{1,2,3,4} 

Although implicated in adhesion, only a few studies address how the actin assembly factors guide cell positioning in multicellular tissues. The formin, Dia1, localizes to the proliferative basal layer of the epidermis. In organotypic cultures, Dia1 depletion reduced basal cell density and resulted in stratified tissues with disorganized differentiation and proliferative markers. Since crowding induces differentiation in epidermal tissues, we hypothesized that Dia1 is essential to reach densities amenable to differentiation before or during stratification. Consistent with this, forced crowding of Dia1-deficient cells rescued transcriptional abnormalities. We find Dia1 promotes rapid growth of lateral cell–cell adhesions, necessary for the construction of a highly crowded monolayer. In aggregation assays, cells sorted into distinct layers based on Dia1 expression status. These results suggest that as basal cells proliferate, reintegration and packing of Dia1-positive daughter cells is favored, whereas Dia1-negative cells tend to delaminate to a suprabasal compartment. This work elucidates the role of formin expression patterns in constructing distinct cellular domains within stratified epithelia.

Introduction

Throughout adulthood, epithelia turn over yet retain distinctive architectures. Such tissues often encompass subdomains distinguished by unique cellular morphology and behavior. The mechanisms, however, by which these domains arise and persist remain a puzzle. Exemplifying the problem, keratinocytes establish stratified structures at the skin surface characterized by layers with distinct morphologies (Luxenburg and Zaidel-Bar, 2019; Simpson et al., 2011). A basal layer of proliferative, columnar cells pack atop a collagenous dermis and give rise to overlying layers with flattened, squamous morphologies. As cells stratify and change shape, a differentiation program ensures that suprabasal cells repress proliferative behavior and express factors required for producing an effective barrier to water loss, pathogens, and mechanical insult (Barrandon and Green, 1985).

Of note, basal cell shape affects the capacity to coordinate stratification with differentiation (Box et al., 2019; Miroshnikov et al., 2017). Reduced cell spread area, concomitant with basal layer packing, also triggers serum-response factor (SRF), Yes-associated protein (YAP) and NOTCH responses which drive differentiation (Connelly et al., 2010; Totaro et al., 2017). Coordination of cell movement with differentiation in these models, however, is contingent upon establishing a densely packed basal layer. The question arises as to how the skin and other stratified

epithelia shunt proliferation into packing the basal layer rather than distributing cells homogeneously throughout the tissue thickness. To compartmentalize tissues, cells sort out based on differential intercellular adhesion and actomyosin contractility (Fagotto, 2014; Maitre et al., 2012; Manning et al., 2010). The segregation of like cells based on these properties guides prominent developmental processes like gastrulation but is also thought to aid in maintaining compartments at homeostasis (Krens and Heisenberg, 2011). In epidermal tissues, genetic studies indicate that cadherin and integrin-based adhesion ensure proper basal layer formation (Brakebusch et al., 2000; Raghavan et al., 2000; Tinkle et al., 2008; Vasioukhin et al., 2001). Similarly, classic in vitro studies indicate that when mixed in a cell aggregate, undifferentiated keratinocytes separate from differentiated neighbors to form compartments (Watt, 1984). Recent studies highlight the differences in basal and suprabasal layer stiffness (Fiore et al., 2020), pointing to mechanics as a likely determinant of this separation.

How actin regulatory proteins, through their effects on cell–cell adhesion and cortical mechanics, enforce compartmentalization of the basal layer is not well understood. Whereas earlier studies implicate depolymerizing agents like cofilin in epidermal function (Luxenburg et al., 2015), the role of actin

¹James Franck Institute, The University of Chicago, Chicago, IL; ²Institute for Biophysical Dynamics, The University of Chicago, Chicago, IL; ³Department of Physics, The University of Chicago, Chicago, IL; ⁴Pritzker School of Molecular Engineering, The University of Chicago, Chicago, IL.

Correspondence to Margaret L. Gardel: gardel@uchicago.edu.

© 2022 Harmon et al. This article is distributed under the terms of an Attribution–Noncommercial–Share Alike–No Mirror Sites license for the first six months after the publication date (see <http://www.rupress.org/terms/>). After six months it is available under a Creative Commons License (Attribution–Noncommercial–Share Alike 4.0 International license, as described at <https://creativecommons.org/licenses/by-nc-sa/4.0/>).

nucleators requires further attention. Disruption of the branched actin nucleator, Arp2/3, or its activator, the WAVE complex, perturbs epidermal function with varying effects on the structure (Cohen et al., 2019; van der Kammen et al., 2017; Zhou et al., 2013). Unbranched actin filaments produced by the formin family anchor adhesions and participate in physiological adaptations to mechanical stretch within the epidermis (Aragona et al., 2020; Kobiela et al., 2004). Endogenous miRNA restricts expression of the canonical formin, Dial, to the basal layer of human epidermis and tongue (Sundaram et al., 2013; Sundaram et al., 2017). Though diabetic ulceration and certain carcinomas yield aberrant expression patterns (Chakraborty et al., 2010; Sundaram et al., 2013; Sundaram et al., 2017; Whitson et al., 2018; Xing and Liu, 2017; Yang et al., 2019), the normal physiological function of Dial in the basal layer remains unclear. One hypothesis is that differential Dial expression translates into differential adhesion effects amenable to packing and producing a properly shaped basal compartment.

In addressing this hypothesis, we found that Dial depletion in a model epidermis disrupted basal layer morphology and led to differentiation defects. Effects on morphology originated from the capacity of Dial to accelerate lateral adhesion growth. In monolayers, this feature allowed cells to accommodate crowding by enabling redistribution of the cortex toward building taller lateral adhesions and smaller basal footprints. Dial depletion, in contrast, forced cells to evade crowding via delamination. Thus, as proliferation added cells to the Dial-positive basal layer, the ensuing rearrangement of junctions favored packing the basal layer over movement into the suprabasal compartment. This effect ensured a density amenable to triggering differentiation. In vitro assays also supported the hypothesis that Dial expression discrepancies can guide cell compartmentalization. In mature stratified epithelia, we posit that the basally skewed expression pattern of Dial establishes a differential adhesion effect which guides redistribution of adhesions during division. Rapid expansion of lateral junctions between Dial-positive neighbors ensures reintegration of basal daughter cells during division. In contrast, crowding of a Dial-negative cell by a neighboring division drives delamination and stratification. Our results provide the first indication that formin expression gradients, through effects on cell sorting, enforce the maintenance of distinct morphological zones within complex tissues.

Results

Dial controls basal layer morphology and packing

Involvement of Dial in immune function and the sensitivity of skin to immunological influence steered us toward the in vitro approach of a well characterized, organotypic culture model (Albanesi et al., 2018; Lin et al., 2011; Peng et al., 2007). To mimic the in vivo juxtaposition of epidermal epithelia to its supporting connective tissue, three-dimensional cultures are produced by plating keratinocytes, like the HaCaT line, upon fibroblast-doped collagen (Schoop et al., 1999). Though they mature slower than primary cell counterparts (Schoop et al., 1999), HaCaT cultures developed at an air-liquid interface construct a stratified tissue with architecture and expression profiles

mimicking those of normal tissues (Koehler et al., 2011; Sundaram et al., 2017). Immunostaining of tissue sections produced from 10-day-old, paraffin-embedded control (CTL) cultures indicated that Dial expression, as well as the shape and orientation of nuclei, changed with respect to position in the stratified tissues. Dial concentrated in the basal layer, approximated as keratinocytes lying within 10 μm of the underlying collagen (dashed line, Fig. 1 A). This localization is consistent with the earlier findings in human epidermis and tongue (Sundaram et al., 2013; Sundaram et al., 2017); we validated the results by Dial staining of skin and tongue samples (Fig. S1). Further, we also found Dial enriched in the basal layer of the hair follicle outer root sheath (Fig. S1).

Basal layer keratinocytes produced a mean linear density of 13 cells per 100 μm (Fig. 1, B and C). Within the basal layer, nuclei are elongated, with an average aspect ratio of 2.5 (Fig. 1, B and C), and are oriented such that the long axis is nearly perpendicular to the basal surface, with the average angle between these axes being 25° (Fig. 1 E). Both the nuclear shape and orientation change in a stereotypical fashion toward the apical surface. As their relative position increases, the nuclei are less elongated but maintain their orientation (Fig. 1, A-E). In the most suprabasal layers, the aspect ratio and orientation increases such that the long axes are parallel to the basal interface (Fig. 1, A-E). Experimental replicates of Fig. 1, D and E are presented in Fig. S2 and demonstrate similar behavior.

To explore the role of Dial on the architecture of stratified tissues, we used CRISPR and shRNA to reduce Dial expression (Fig. S3). Both techniques diminished Dial expression, with shRNA yielding knockdown efficiencies of 65–80% and CRISPR edits causing near total abrogation of Dial protein levels. Next generation sequencing identified two frameshift variants with premature stop codons, accounting for ~85% of the genomic sequencing signal (Fig. S3). Tissue depleted of Dial by CRISPR (DialKD) stratified but produced a basal layer that was 20% less dense than CTL cells and lacked the stereotypical, columnar morphology (Fig. 1, A and C). Within the basal layer, the nuclei of DialKD cells were less elongated and randomly oriented, at times lying parallel to the underlying collagen (Fig. 1, A, D, and E; and Fig. S2). The nuclear shape remained constant in the suprabasal layers and showed a similar trend toward becoming parallel to the basal interface at high relative positions (Fig. 1 E). Multicellular patches of DialKD cells were also observed protruding into the underlying collagen (Fig. S3).

To overcome the limitations of measuring two-dimensional (2D) density in a cross section, we conducted confocal imaging of flat mounted, H2B-labeled cells (CTL-H2B and DialKD-H2B) cultured for 6 days (Fig. 1 F). These data revealed similar basal layer density deficits in DialKD-H2B cells (Fig. 1 G) and was corroborated by flat-mounted imaging of fixed cultures (Fig. S4). Dial-depleted tissues successfully stratified but did so without producing a properly packed basal layer, leading us to posit that cells were escaping the basal layer before reaching an appropriate density.

Dial expression supports epidermal differentiation

Since morphology dictates the success with which basal cells differentiate (Connelly et al., 2010; Totaro et al., 2017), we next

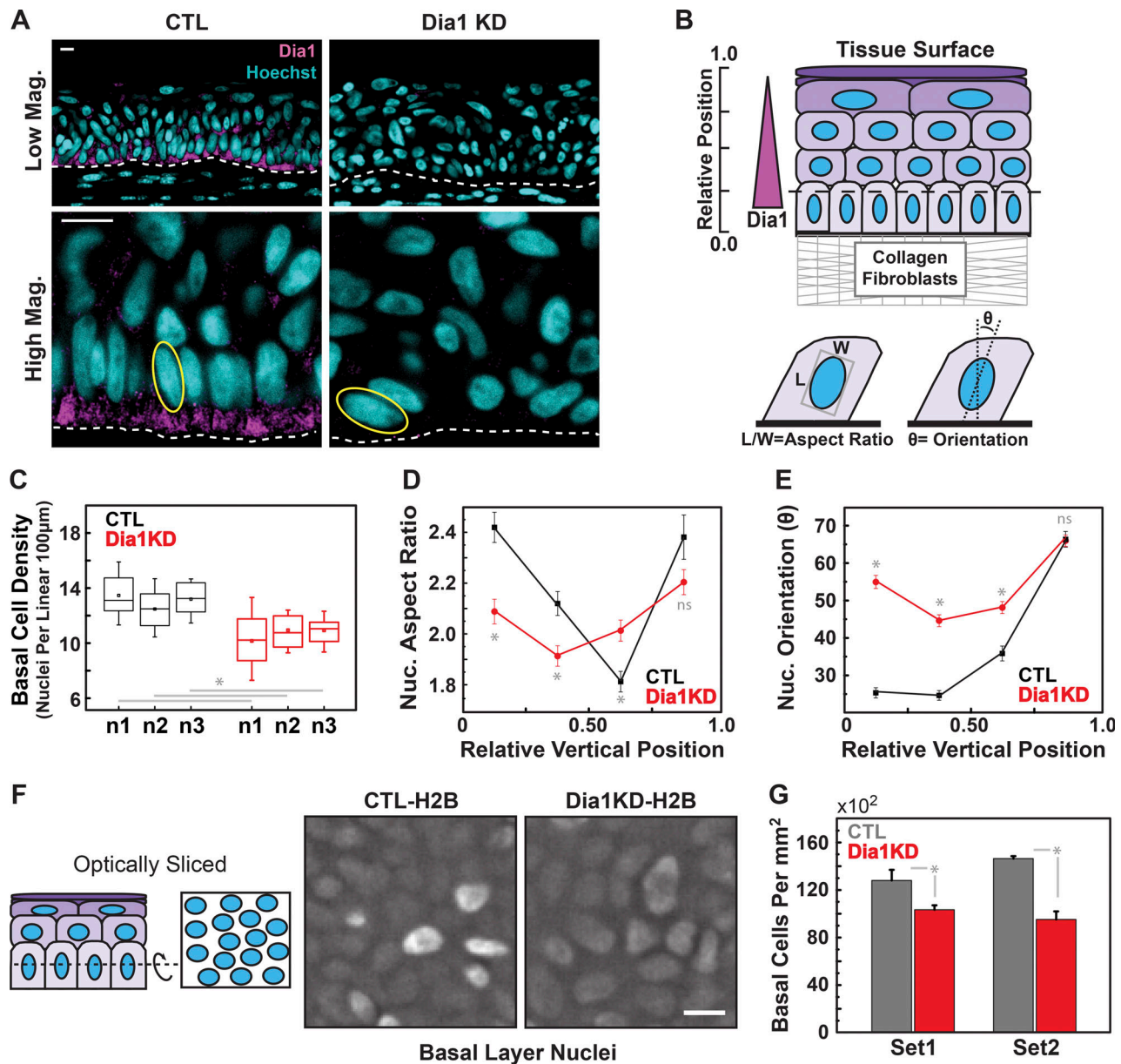


Figure 1. Dia1 supports basal layer packing in stratified tissue. (A) Immunohistochemical staining of Dia1 in cross sections obtained from paraffin-embedded cultures, fixed 10 days after lifting to an air-liquid interface. Scale bars = 10 μ m. Example of fit ellipses used for subsequent measurements indicated in yellow. Dotted line separates keratinocytes from the underlying collagen and fibroblasts. (B) Schematic illustrating measurements taken from tissue cross sections and presented in C–E. (C) Linear density of basal nuclei, 20–27 images analyzed per sample. (D) Aspect ratio of nuclei as a proxy for cell shape throughout tissue thickness. (E) Orientation of nuclei throughout the tissue thickness with respect to the keratinocyte–collagen border. For D and E, plotted points represent the mean \pm SEM of data derived from 85 to 235 nuclei lying within bins bounded by x-axis ticks for a single sample set. Two additional experiments are shown in Fig. S2. (F) Optical sectioning of basal nuclei in live 3D cultures carrying GFP-labeled H2B, 6 days after lifting to an air-liquid interface. Images are average projections of confocal slices extending 6 μ m above the most basal, in-focus plane of H2B signal, and filtered to remove background. Scale bar = 10 μ m. (G) Mean density of basal nuclei obtained from optical sectioning \pm SEM. Data represent 5–6 fields per condition from two independent experiments. For C, boxes = 25–75th percentile, whiskers = 10–90th percentile, square = mean and line = median. Two-tailed, independent Student’s *t*-test results are indicated as: $P < 0.05$ (*), $P > 0.05$ was considered not significant (ns). For G, the *P*-value was calculated using a two-tailed Mann–Whitney *U*-test.

tested whether the aberrant morphology caused by Dia1 depletion impacted epidermal differentiation. To address this possibility, sections of organotypic cultures were immunohistochemically stained for the differentiation marker, keratin-10 (KRT10). As in normal tissue, CTL cells produced a three-dimensional culture in which KRT10 localized specifically to suprabasal layers (Fig. 2, A

and B). Dia1KD cells, conversely, produced tissues that stratified but contained lesions of KRT10-negative cells (Fig. 2, A and B). Organotypic cultures derived from shRNA-treated cells (shCTL and shDia1) corroborated these results (Fig. S3).

Spatially segregated proliferation is an important attribute of differentiation in stratified tissues, and its loss is linked to

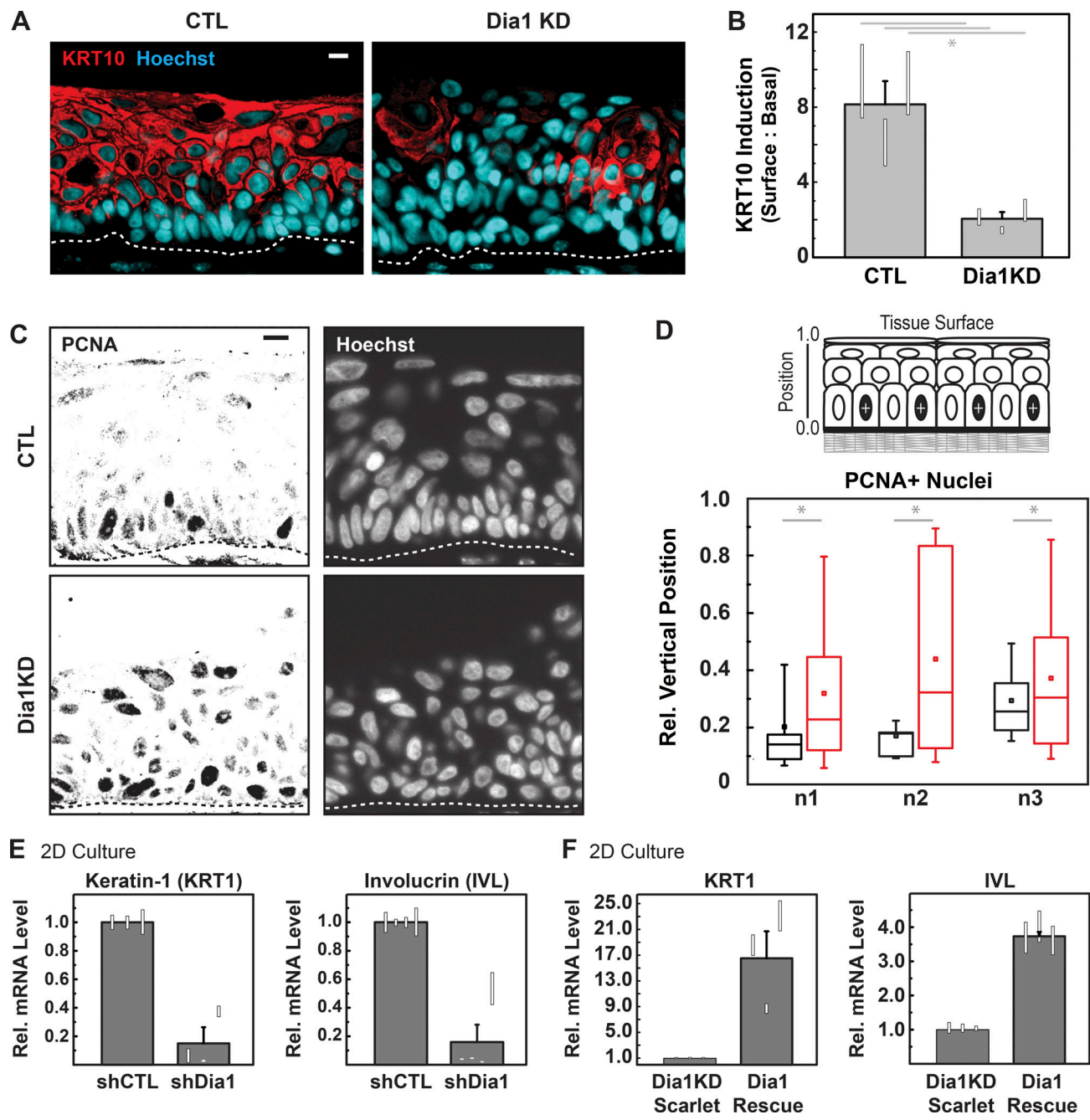


Figure 2. Dia1 supports epidermal differentiation. (A) Keratin-10 (KRT10) staining of cross sectioned, paraffin-embedded 3D cultures. (B) Induction of KRT10 expressed as the ratio of cytoplasmic KRT10 signals obtained from cells at the tissue surface and basal layer in a given field. Results represent three independent experiments. To compare CTL and Dia1KD cultures, 15 vs. 20, 20 vs. 20, and 27 vs. 26 fields were analyzed in n1, n2, and n3, respectively. Column graph indicates mean of the three experiments \pm SEM. White boxes represent 25–75 percentile range of samples from each experiment. Each individual experiment was subjected to a two-tailed, independent Student’s *t*-test. (C) PCNA staining of paraffin sections. (D) Distribution of PCNA+ cells with respect to vertical position in the epidermis. PCNA+ = 1.5 fold greater signal than control, suprabasal nuclei for three independent experiments. 755 vs. 989, 281 vs. 335, and 859 vs. 862 nuclei were analyzed for CTL and Dia1KD cultures in n1, n2, and n3, respectively. (E) Effects of shRNA-mediated Dia1 depletion on differentiation marker expression 48 h post-calcium addition in 2D culture. Results represent the mean of 3–4 biological replicates \pm SEM. 95% CI of technical replicates for each experiment are indicated by white boxes. (F) Differentiation induction at 48 h by ectopic mDia1 introduced to Dia1KD cells. Results represent the mean of three biological replicates \pm SEM. 95% CI of technical replicates for each experiment are indicated by white boxes. For A and B, scale bars = 10 μ m; dashed line = approximate collagen boundary. For C and D, boxes = 25–75th percentile, whiskers = 10–90th percentile, square = mean, line = median. Two-tailed, independent Student’s *t*-test results are indicated as $P < 0.05$ (*).

pathologies ranging from barrier disruption to viral oncogenesis (Moody and Laimins, 2010; Rorke et al., 2015). Staining for the proliferation marker, proliferating cell nuclear antigen (PCNA), allowed for visualization of where proliferative cells reside in the stratified layers. Control tissues demonstrated proper restriction of proliferative cells to the basal layer (Fig. 2, C and D). Dial-depletion led to the extension of PCNA positive cells throughout the tissue thickness (Fig. 2, C and D). Further, the percentage of PCNA positive nuclei was 18% in the DialKD cells, reflecting a sixfold overall increase from that of control tissues (2.9%). This is reminiscent of hyperproliferative phenotypes associated with stratified tissue disorders such as psoriasis and esophageal disease (Hugh and Weinberg, 2018; Wang et al., 2005).

Standard 2D culture methods of assessing differentiation corroborated the organotypic model results. A well-known technique for inducing differentiation *in vitro* entails culturing cells confluent in low calcium (0.03–0.07 mM CaCl₂), then switching the cells to a high calcium (1.2–2.8 mM) media (Deyrieux and Wilson, 2007). Compared to shCTL-treated cells, the mRNA level of differentiation markers involucrin (IVL) and keratin-1 (KRT1) were diminished fivefold in shDial cells (Fig. 2 E). To validate the specificity of this result, we transduced DialKD cells with a Scarlet-tagged, full-length mouse Dial, referred to hereafter as Dial-Rescue cells (Fig. S5). Compared to Scarlet-only controls (DialKD-Scarlet), reintroduction of Dial facilitated induction of IVL and KRT1 expression in this simplified assay (Fig. 2 F). These results confirmed the specificity of differentiation abnormalities stemming from Dial depletion.

Forced crowding rescues transcriptional abnormalities in Dial-deficient cells

To assess the impact on transcriptional changes expected during stratification, we assessed differential gene expression in confluent DialKD-Scarlet cells compared to the Dial-Rescue line via RNAseq. Of the 15,150 genes detected, ~275 of these were upregulated at least twofold in the rescue line (Fig. 3 A). Strikingly, the top five gene sets enriched by Dial rescue, as detected by automated gene ontology, were those of cornification, keratinization, keratinocyte differentiation, and epidermal differentiation/development. Although highly overlapping sets, these strongly implicated Dial in epidermal development.

We then performed a manual query of this data with published gene sets for skin differentiation (Joost et al., 2016), skin disease (Lemke et al., 2014), and genes driven by salient pathways like p63 (Truong et al., 2006), YAP (Wang et al., 2018), or NOTCH signaling (Wang et al., 2014). Genes linked to skin disease, differentiation, p63, or NOTCH signaling increased in response to Dial rescue (Fig. 3 B). In particular, we observed increased expression of the small proline-rich (SPRR) proteins (Fig. S6), essential for cornification (Carregaro et al., 2013). In contrast, several notable YAP target genes decreased in response to rescued Dial expression. Targets of other signaling programs salient to differentiation like SRF (Olson and Nordheim, 2010), SHH (Lewandowski et al., 2015) and Wnt (Watanabe et al., 2014) did not demonstrably trend toward up- or downregulation, but contained individual transcripts displaying sensitivity to Dial expression (Fig. 3 B and Fig. S6). Altogether, this data underscored

that Dial expression, even in *in vitro* culture models, could drive gene expression signatures pertinent to *in vivo* epidermal differentiation.

To determine whether aberrant cell area and/or density contributed to the differentiation phenotype of Dial-deficient cells, we explored whether enforced crowding could rescue transcriptional abnormalities. Inspired by an earlier study (Miroshnikova et al., 2017), keratinocytes were seeded on biaxially pre-stretched (36% by area) PDMS sheets. After incubating cells for 20 h, stretch was released, in effect, increasing cell density (Fig. 3 C). Sampled at the center of the culture area, release from stretch increased DialKD-Scarlet density by ~50% from 2,455 to 3,645 cells per mm² (Fig. 3 D). By comparison, a parallel Dial-Rescue culture produced a mean cell density of 2,755 cells per mm² (Fig. 3 D). Thus, relaxing prestretch provided a means to enforce crowding of Dial-deficient cells into densities beyond those achieved by unmanipulated Dial-Rescue cells. Mitigating the prestretch to 18% and, in turn, dampening the extent of cell density increase, enabled achievement of densities more closely mimicking those of Dial-Rescue cultures (Fig. S7). Following 5 h of incubation post-release, samples were collected for RNA sequencing (Fig. S5). DialKD-Scarlet cells with and without enforced crowding were compared to identify differentially expressed genes. Interestingly, we saw enhanced expression of the 276 Dial-driven genes identified in Fig. 3 A for both levels of enforced crowding. Similarly, we saw reduced expression of Dial-inhibited genes. This appeared specific to Dial-responsive genes, as randomly chosen gene sets demonstrated little response to crowding (Fig. 3 E).

Manual inspection of transcripts from Fig. 3 E that were at least 1.6× enriched or depleted identified a number of differentiation markers as well as components of the pro-differentiation p63 and Notch pathways (Fig. 3 F). GSEA database analysis revealed that both Dial expression and enforced crowding of DialKD-Scarlet cells suppressed nonepidermal (neural; GO:0007417, GO:0022008) gene expression, specifically among targets of Polycomb Repressive Complex 2 (PRC2)-mediated silencing (Ben-Porath et al., 2008). This set included two YAP-activated genes, TGFB2 and SLIT2, which tracked with connective tissue growth factor (CTGF) in responding negatively to crowding (Cordenonsi et al., 2011; Wang et al., 2018). Consistent with reports of YAP antagonizing differentiation (Totaro et al., 2017; Zhou et al., 2013), both crowding and Dial rescue upregulated expression of differentiation markers including DAPL1, DSC1, and CERS3. At this timepoint, crowding does not induce upregulation of the classic epidermal differentiation marker, KRT1. However, by increasing the incubation time to 9 h after releasing prestretch, we were able to detect an upregulation of KRT1 via qPCR within DialKD-Scarlet cells (Fig. S8). The crowding-induced upregulation of CERS3, an enzyme crucial to epidermal function (Jennemann et al., 2012), and downregulation of CTGF, a marker of YAP activity (Wang et al., 2018), were, likewise, corroborated by qPCR. When performed on subconfluent cultures, enforced crowding failed to induce KRT1 and CERS3, suggesting that induction did not arise solely from a transient drop in cellular tension but required dense culture conditions (Fig. S8). Together, the data indicated that Dial-dependent effects on basal layer crowding contributed to keratinocyte differentiation.

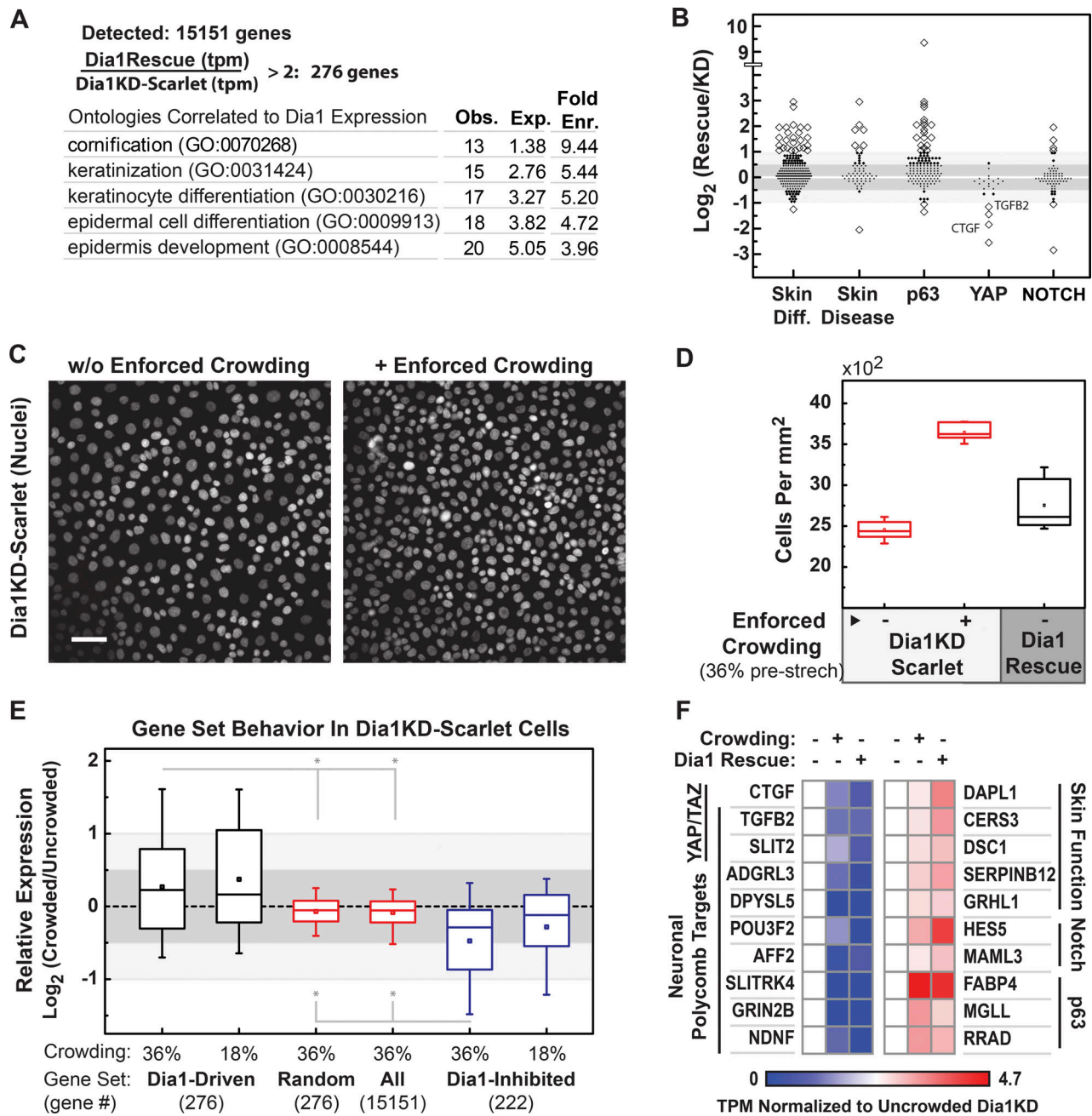


Figure 3. Crowding rectifies transcriptional defects associated with Dia1-deficiency. (A) Gene ontology analysis of genes identified by RNAseq as being upregulated more than twofold in response to ectopically expressed mDia1 in Dia1KD cells. Each dot reflects the fold-enrichment/depletion of a single gene from duplicate experiments. (B) Log_2 fold change analysis of Dia1KD-Scarlet cultures compared to Dia1-rescue cells with respect to published gene sets tracking differentiation, monogenic skin disorders, genes induced by p63, YAP/TAZ, and NOTCH signaling. Prominent YAP targets are noted. (C) Cells plated on biaxially stretched PDMS (36% by area) were released from stretch to force cell crowding. Images depict nuclear staining of uncompressed and compressed cells immediately after releasing stretch. Parallel cultures were incubated a further 5 h and processed for RNAseq. (D) Crowding quantified in terms of cell density with and without forced crowding. 30 fields per condition. (E) Behavior of genes identified as Dia1-responsive (induced or inhibited more than twofold by Dia1 rescue in A within Dia1KD-Scarlet cells subjected to crowding. (F) Effect of crowding versus Dia1 rescue on genes belonging to salient signaling groups within Dia1KD-Scarlet cells in the 36% prestretched sample. Expression analyses are based on TPM (transcripts per million) normalizations. Scale bars = 50 μm . Box plots = 25–75 percentile, whiskers = 10–90th percentile, line = median, square = mean. Two-tailed, independent t-test results of $P < 0.05$ (*) are indicated.

Dia1 expression controls the density at which cells stratify

To explore the formation of stratified tissue, we used live cell imaging to monitor the onset of suprabasal layer production in cultures of GFP-H2B marked cells plated atop fluorescently labeled collagen (Fig. 4 A and Fig. S9). CTL-H2B and Dia1KD-H2B

cells initially formed monolayers (Fig. 4 A). At 24 h, basal layer density in CTL-H2B cultures increased by twofold, accompanied by the onset of a suprabasal layer (Fig. 4, A and B). Over the next 75 h, the basal layer density remained constant, whereas the number of suprabasal cells continued to increase (Fig. 4, A and

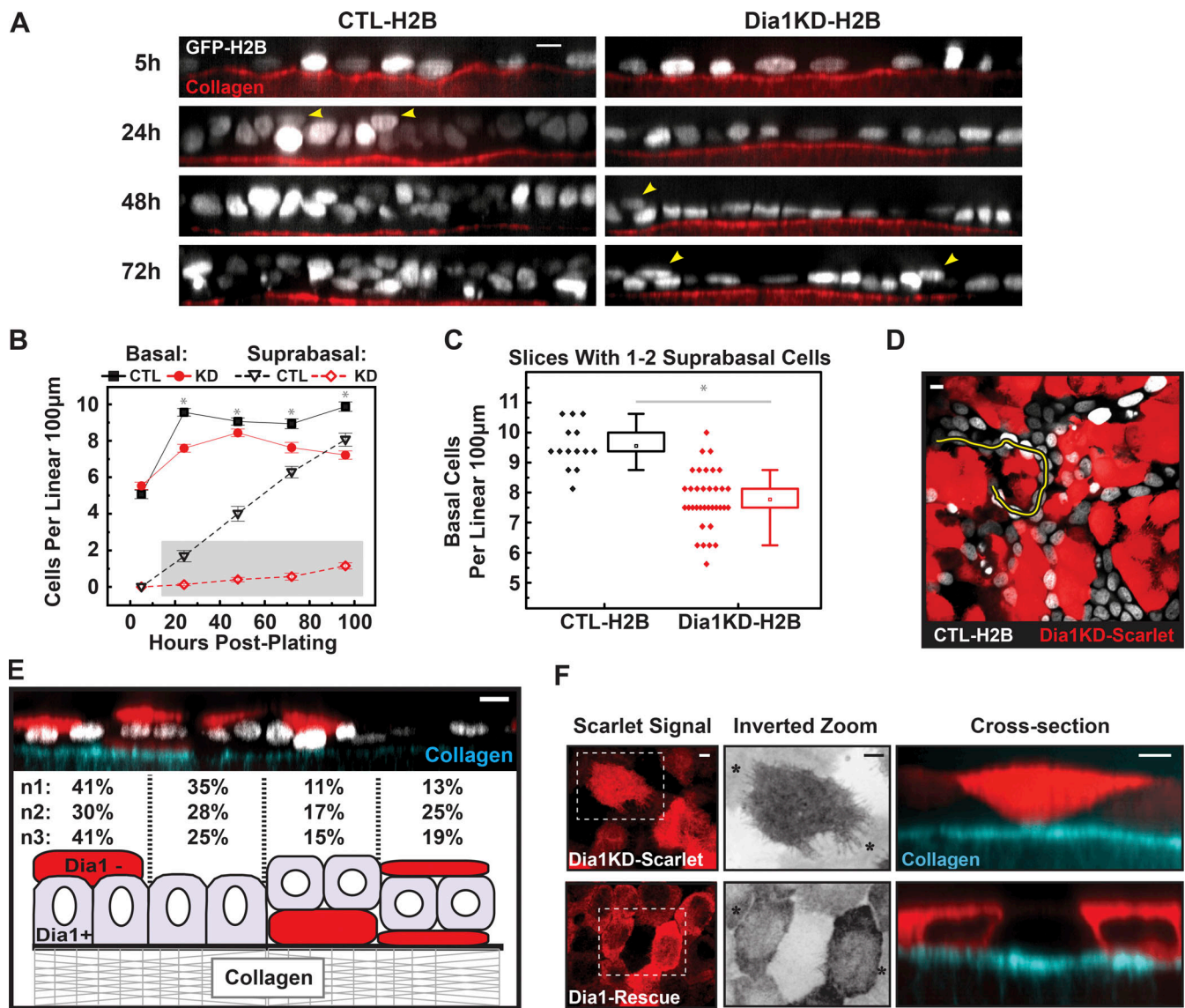


Figure 4. Dia1 expression controls the density at which cells protrude and migrate atop neighbors. (A) Orthogonal slices, averaged across 5 µm thicknesses, of live, GFP-H2B marked cells, plated upon labeled collagen gels for the indicated times. Yellow arrowheads = suprabasal cells. (B) Counting of basal and suprabasal cells per orthogonal slice with respect to time since plating. 20 orthogonal slices per condition per timepoint were analyzed. H2B signals occluding >50% of an underlying H2B signal or overlying multiple H2B-labeled nuclei were considered suprabasal. Plotted values represent the mean per slice ± SEM. Gray region: data pertaining to C. (C) Linear density of basal cells in z-slices, limited to slices containing only 1–2 suprabasal cells per 100 µm, regardless of timepoint. Diamonds = individual slices (CTL: 14 slices, Dia1KD: 35 slices). Boxes = 25–75th percentile, whiskers = 10–90th percentile, square = mean. A duplicate experiment pertaining to C and D is found in Fig. S9. (D) Mixed cultures containing CTL-H2B cells (white) and Dia1KD-Scarlet cells (red) at 96 h post-plating. Image of basal layer cells. Yellow line pertains to E. (E) Orthogonal slice along CTL-H2B nuclei bordering a Dia1KD-Scarlet region marked by yellow in D. Frequencies of illustrated spatial relationships between CTL-H2B and Dia1KD-Scarlet cells at boundary regions. Values represent frequencies of three independent experiments, each encompassing 100–400 CTL nuclei. (F) Maximum projections of the top 2 µm of confocal slices capturing Scarlet and Scarlet-tagged mDia1 in Dia1KD-Scarlet and Dia1-rescue cells, respectively. Inverted zoom depicts boxed regions in left panels, cross sections were taken between the asterisk marks in the inverted panels. Scale bars = 10 µm for A, D, and E; 5 µm for F. Two-tailed, independent Student’s *t*-test results are indicated where *P* < 0.05 (*). In B, *t* tests were conducted on basal cell density values.

B). In comparison, Dia1KD-H2B cells populated the culture at a reduced rate, possibly due to slower rates of proliferation (Fig. 4 B and Fig. S10). The basal layer achieved a steady-state density around 24 h post-plating, albeit 20% lower than that of CTL-H2B cells (Fig. 4 B). On the surface, this reduced proliferation is in apparent contrast with the hyperproliferative phenotype shown in (Fig. 2 C). However, the data in Fig. 2 C were acquired several days after forming 3D organotypic cultures, and we suspect

arises from a failure in Dia1KD tissues to repress proliferation, consistent with a differentiation defect.

Though cells were observed in the Dia1KD-H2B suprabasal layer, the basal layer density was significantly reduced at all times. To measure the basal layer density corresponding to the onset of suprabasal layer formation, we measured the linear cell density in regions proximal to instances with 1–2 suprabasal cells per 100 µm. Consistent with our earlier results, the linear

density of the basal cell layer was 20% reduced in DialKD cells compared to the control cells (Fig. 4 C and Fig. S9). Thus, Dial-deficient cultures stratified but did so later and with lower basal cell densities.

Dial expression is sharply attenuated in the suprabasal cells of control tissues. We wished to explore whether this segregation would spontaneously occur in mixed cultures of DialKD and CTL cells. We produced mixed cultures containing even portions of DialKD cells expressing the fluorescent protein Scarlet, marking the cytoplasm, with CTL-H2B cells. After 4 days of growth on collagen gels, confocal imaging was used to assess the spatial relationship between DialKD-Scarlet and CTL-H2B cells (Fig. 4 D). The two cell types did not readily mix; CTL-H2B cells formed strands of connected islands weaving in between Dial-negative regions (Fig. 4 D). We assessed the lateral positioning of the cells by imaging orthogonal sections of three independent trials (Fig. 4 E). In control cultures at similar time points, we would expect all cells to have suprabasal partners at this time-point (Fig. 4, A and B). However, we found that 25–35% of control cells lacked suprabasal partners (Fig. 4 E). For those that did have a suprabasal partner, we found that 30–41% of CTL-H2B cells had acquired DialKD-Scarlet cells as suprabasal neighbors, whereas 11–17% of CTL-H2B cells had assumed a suprabasal position overlying a DialKD-Scarlet cell (Fig. 4 E). In 13–25% of cases, CTL-H2B cells wedged between two layers of DialKD-Scarlet cells (Fig. 4 E). These data indicated that DialKD-Scarlet cells preferentially localize to the suprabasal compartment when challenged by CTL-H2B cells.

This point becomes strikingly clear when DialKD-Scarlet cells are more heavily diluted among CTL-H2B cells (1:50; Fig. S11). Here, the cell density is largely controlled by the CTL-H2B cells, and we found that DialKD-Scarlet cells are found in suprabasal layers (Fig. S11). This suggests that Dial-negative cells were intolerant of densities produced by Dial-positive cells, leading to basal layer egress. We noted here that inhibiting ROCK, an upstream activator of myosin that cooperates with Dial to produce contractile actomyosin networks, blunted preferences for the suprabasal compartments and yielded monolayered cultures. In monocultures, 24% of CTL-H2B cell divisions orient perpendicular to the underlying collagen compared to 6% of DialKD-H2B divisions (Fig. S12). This is consistent with the lower cell density achieved by DialKD-H2B cells and with published work (Box et al., 2019) indicating that cell density controls division orientation. This argued against the idea that DialKD cells populate a suprabasal compartment by shifting to asymmetric divisions at an abnormally low density. Thus, we turned our attention to stratification by delamination as a suitable context within which to examine the apparent sorting of DialKD cells into the suprabasal compartments.

To understand how this sorting occurred, we then considered how Dial expression impacted the cross-sectional shape of cells, as a means of inferring the likelihood of apical protrusion. A previous study noted that Diaphanous depletion in *Drosophila* led to enhanced apical cross sections, consistent with increased apical protrusion (Homem and Peifer, 2008). To facilitate this assay, we formed monolayers and exploited the cytoplasm outlines produced by Scarlet and Scarlet-mDial signals in DialKD-

Scarlet and Dial-rescue cells, respectively. Immunofluorescence of fixed cells revealed enhanced spreading and protrusion of DialKD-Scarlet cells both atop and below neighbors (Fig. 4 F). The wedge-shape associated here with Dial-deficiency mimicked morphology marking the delamination and protrusion of keratinocytes into the suprabasal layer during stratification (Miroschnikova et al., 2017). Together, the results supported a hypothesis that heterotypic interactions between Dial-positive and negative cells guided the protrusive activity of Dial-negative cells toward the suprabasal compartments. The resulting arrangement mimicked the spatial relationship observed in vivo.

Differential Dial1 expression drives cell sorting

The observed changes in cell morphology implicated Dial in modifying cell adhesion and/or cortical mechanics. To query this, we used immunofluorescence to visualize the actin and collagen in the vertical cross section of newly forming adhesions between CTL or DialKD cells 4 and 20 h post-plating (Fig. 5 A). We observed, at 4 h post-plating, that nascent cell-cell contacts between CTL cells induced distortion of the underlying collagen; this was not observed at 20 h (Fig. 5 B). This matrix distortion is accompanied by the production of phospho-myosin decorated, perijunctional actin filaments (Fig. S13), consistent with a role of formin-dependent actin assembly supporting cortical tension (Acharya et al., 2017; Bovellan et al., 2014; Harris et al., 2014). Indeed, nascent cell-cell contacts formed by DialKD cells did not distort the underlying collagen at either 4 or 20 h (Fig. 5, A and B), failed to produce the perijunctional actin pool and possessed modestly diminished overall levels of phospho-myosin (Fig. S13). This did not correspond to an overall reduction in F-actin intensity, but rather represented changes in the organization of F-actin. However, at 4 h, DialKD cells failed to extend their junctions vertically to match the plane of the cell apex, particularly at sites of tricellular junctions (Fig. 5 C and Fig. S13). Thus, whereas CTL cultures produced monolayers with flat apical surfaces, those of DialKD cultures slightly undulate. Measurement of contact angles at the apical and basal planes of cell junctions revealed larger, flatter angles at the apical junctions of CTL cultures when compared to those obtained from the basal surface (Fig. 5, D and E). DialKD cells produced an opposite effect. This indicated that cortical tension along the apical surface exceeded that along the basal surface in CTL cells, characteristic of a mature epithelium. DialKD failed to do so, demonstrating a delayed capacity to mechanically integrate apical cell surfaces during epithelial maturation.

These data suggested that, in CTL cells, force produced along the apical surface was transmitted between cells at the apical junction as well as down the lateral membrane into the collagen. Indeed, examination of E-cadherin staining revealed a discontinuous staining pattern at the apical surface in DialKD cells when compared to CTL cultures, arising from failure of cells to extend junctions vertically (Fig. S14). However, when limiting analysis to the most apical patch of nascent junctions, though discontinuous, mean E-cadherin intensity was not notably diminished in DialKD cells. Consistent with the idea that junctions may exist under tension at this timepoint in CTL cells, there was a modest recruitment of vinculin to E-cadherin

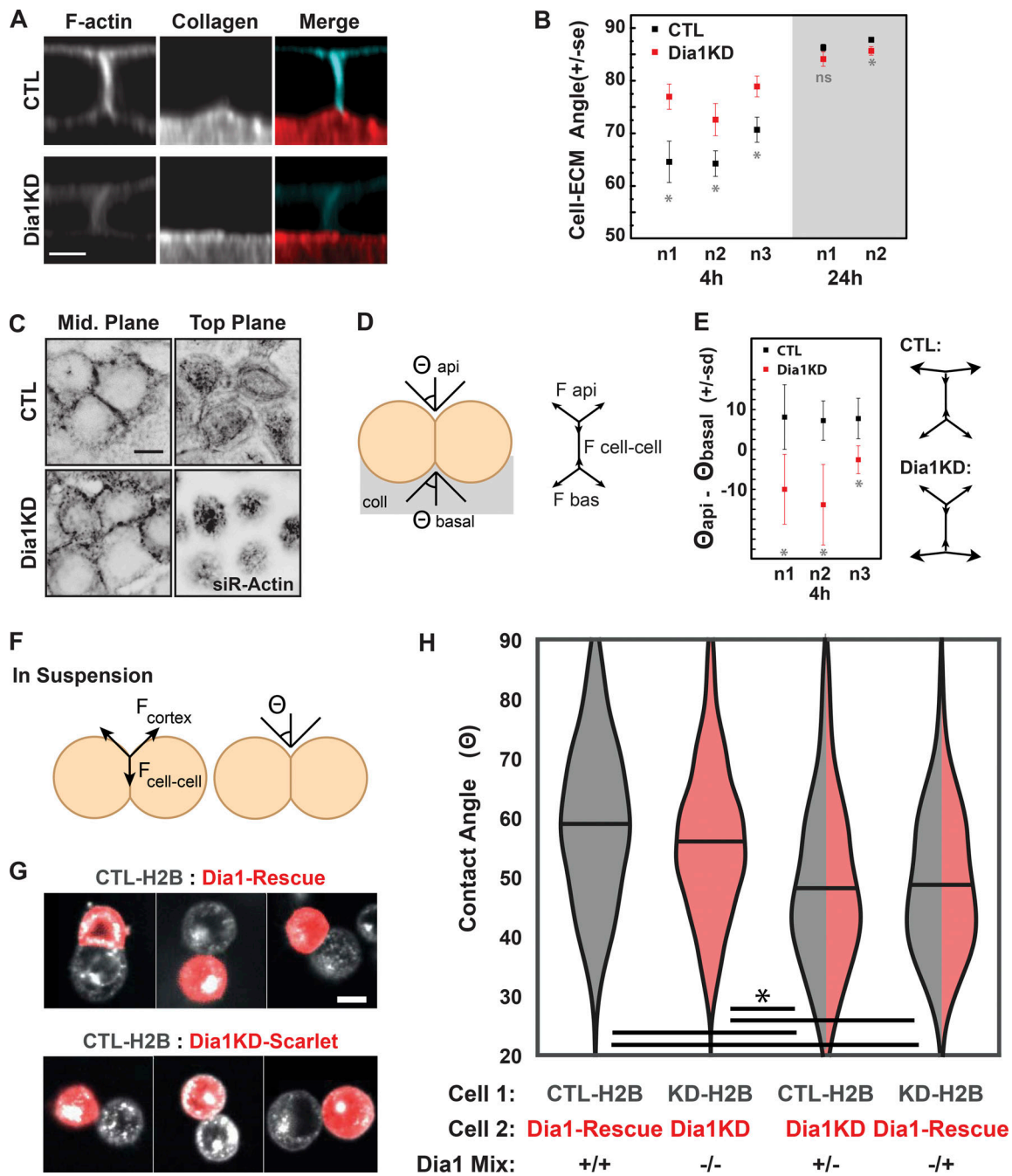


Figure 5. Differential Dia1 expression disrupts adhesion expansion at heterotypic junctions. (A) Orthogonal view of forming junctions, 4 h post-plating upon labeled collagen. (B) Mean value (\pm SEM) of angle formed by collagen deformation between neighboring cells. Angle is divided by two to conform with contact angle conventions. About 20 cell pairs were analyzed per condition for three and two independent experiments at 4 and 20 h, respectively. (C) SiR-actin stain of planes taken through the center and top of cells 4 h post-plating. (D) Diagram illustrating the relationship between apical and basal contact angles with forces along the apical and basal aspects of the cell cortex. (E) Mean difference (\pm SD) of angles measured at the apical and basal ends of intercellular junctions and illustration of qualitative, inferred force balances. A total of 20 junctions were measured per condition for three independent experiments. (F) Diagram of suspended cell doublets indicating how the balance between forces at adhesive ($F_{\text{cell-cell}}$) and nonadhesive (F_{cortex}) portions of the cortex impact contact angles (Θ). (G) Examples of doublets formed between two Dia1-expressing cells (CTL-H2B and Dia1-rescue) versus those formed between Dia1 expressors and nonexpressors (CTL-H2B and Dia1KD-Scarlet, respectively). (H) Contact angle quantitation of doublets formed between the indicated cell types. Violin plots indicate the median (line) derived from cell doublets pooled from three independent experiments. $n = 338, 347, 340,$ and 322 doublets from left to right. Note, the indicated significant differences (*) were also present within each underlying experiment and each condition contained ~ 100 doublets within individual experiments. Two-tailed, independent Student's t -test results are indicated, where $P < 0.05$ (*). Scale bars: $5 \mu\text{m}$ in A, $10 \mu\text{m}$ in C and G.

positive plaques in these cultures. DialKD cells failed to execute this recruitment.

Though suggestive, the contact angle measurements and immunostaining experiments described above cannot clearly describe the distribution of force along the cortex at cell-cell contacts and contact free sites. To isolate these effects, we measured contact angles formed between cell doublets in suspension, to remove contributions made by adhesion to collagen. Doublets formed between CTL-H2B and Dial-rescue cells produced similar contact angles to those produced by DialKD-H2B/DialKD-Scarlet doublets (Fig. 5, F-H). This suggested that, to some extent, adhesion to collagen exacerbated the inability of DialKD cells to increase apical contact angles. Heterotypic mixtures of CTL-H2B/DialKD-Scarlet or DialKD-H2B/Dial-rescue, intriguingly, produced significantly lower contact angles when compared to homotypic interactions. Thus, in contexts where both Dial-positive and Dial-negative cells are present, heterotypic junctions fail to develop as robustly as homotypic interactions. This observation, and prior literature (Canty et al., 2017), led us to hypothesize that heterotypic interactions might elicit separation of Dial-positive and Dial-negative cells into distinct compartments.

In matrix-free cell sorting assays, differential tension and adhesion can drive the separation of distinct cell populations (Foty and Steinberg, 2005; Maitre et al., 2012). We sought to explore whether sorting of CTL and DialKD cells would also occur in a hanging drop assay (Foty and Steinberg, 2005). To form aggregates, CTL cells were mixed 1:1 with DialKD cells and suspended from petri dish lids in drops of media. Mixtures totaling 1,000 or 20,000 cells were tested. To distinguish populations, cell lines carrying the GFP, nuclear label (CTL-H2B or DialKD-H2B) were mixed with those carrying the Scarlet, cytoplasmic labels (CTL-Scarlet or DialKD-Scarlet). After 20 h, confocal microscopy enabled detection of local maxima in z-slices and networks of nearest neighbors were drawn for each signal. CTL-H2B and DialKD-Scarlet cells separated within such aggregates, yielding networks that intersected seldom compared to those constructed from randomized positions (Fig. 6 A). In contrast, there was a high degree of overlap between networks derived from aggregates containing mixtures of CTL-H2B and CTL-Scarlet cells (Fig. 6 B). To quantify separation, the number of intersections determined per z-slice from randomized networks was divided by the number of actual, observed intersections. Thus, randomly distributed mixtures would yield a separation index of 1 with higher values representing a greater degree of separation. Analyzing 10 z-slices per aggregate indicated that CTL/DialKD mixtures (mean index = 1.40 ± 0.13 SE, $n = 21$) displayed significantly ($P = 0.04$) higher levels of separation than CTL/CTL mixtures (mean index = 1.00 ± 0.05 SE, $n = 11$).

Though Dial coordinates with ROCK-dependent myosin activity to generate tension along intercellular contacts (Acharya et al., 2017), treatment of CTL/DialKD mixtures with the Y-27632 ROCK-inhibitor had little impact on the separation index (mean index = 1.41 ± 0.17 SE, $n = 12$). However, inspection of 3D structures revealed a key distinction between untreated and inhibitor-treated mixtures. In large aggregates (20,000 cells),

Dial-positive and negative cells separated into stratified layers, remarkably, mimicking the arrangement of cells in actual stratified tissue (Fig. 6 C). Cells in the presence of ROCK-inhibitor continued to sort but did so horizontally within monolayered aggregates. This could represent local clonal expansion. Alternatively, differential Dial expression may drive cell sorting independent of ROCK but rely on ROCK-dependent myosin activity to establish a stratified arrangement. Indeed, ROCK inhibition blunted the suprabasal movement of DialKD-Scarlet cells when diluted 50-fold into CTL-H2B cells and allowed to adhere to collagen gels (Fig. S11). We concluded that when presented with Dial-negative counterparts, Dial-positive cells preferentially adhere to each other and that addition of ROCK activity drives this separation into a multilayered structure.

Differential Dial1 expression guides adhesion rearrangement following division

Division in the basal layer figures prominently among events which affect cell position in the epidermis (Lechler and Fuchs, 2005; Miroshnikova et al., 2017). In light of the cell sorting data, a reasonable scenario would apply the given role of Dial in building tension-bearing actin networks at adherens junctions (Acharya et al., 2017) toward remodeling events associated with division (Higashi et al., 2016). Static analyses also indicate that Dial supports lateral adhesion height (Carramusa et al., 2007), suggesting that it may aid in rebuilding lateral adhesions following cytokinesis. To test whether Dial expression affected the rate of cell-cell contact expansion, the behavior of nascent cell-cell contacts was observed. CTL or DialKD cells, labeled with siR-actin, were imaged immediately after plating ($t = 0$ min) to capture the formation of cell-cell interfaces along the apical-basal direction. In control cells, the adhesive interface of the lateral membrane domain expanded over the first 4 h, increasing to $7 \mu\text{m}$ in height and increasing the angle formed between cell apices at the top of the contact (Fig. 7, A and B; and Fig. S10). By contrast, in DialKD, the adhesive interface failed to expand over the first 4 h (Fig. 7, A and B). This result represented one of the first attempts to visualize a Dial-dependent effect on lateral membrane growth kinetics. Reintroducing mDial to DialKD cells (Dial-rescue) also accelerated the accumulation of actin at nascent junctions visualized in the XY plane as early as 1 h post-plating (Fig. S10). As cells must reallocate adhesive surfaces following division, these data argued in favor of Dial expression possibly guiding division-associated rearrangements by favoring an actin-driven expansion of interfaces between Dial-positive siblings.

The extent to which adhesion kinetics affected division-associated rearrangement was explored by live imaging of mixed cultures. Juxtaposition of H2B-marked cells with neighbors carrying Scarlet-marked cytoplasm enabled tracking of cell-cell and cell-matrix interfaces during cell division. In all mixtures tested, neighboring cells responded to division by entering the space formerly occupied by the dividing cell, often at the cytokinetic furrow (Fig. 7 C). We predicted that, when presented with the option of reintegrating with a Dial-positive sister or a Dial-negative neighbor, differential adhesion would favor rapid reintegration of CTL-H2B daughter cells and

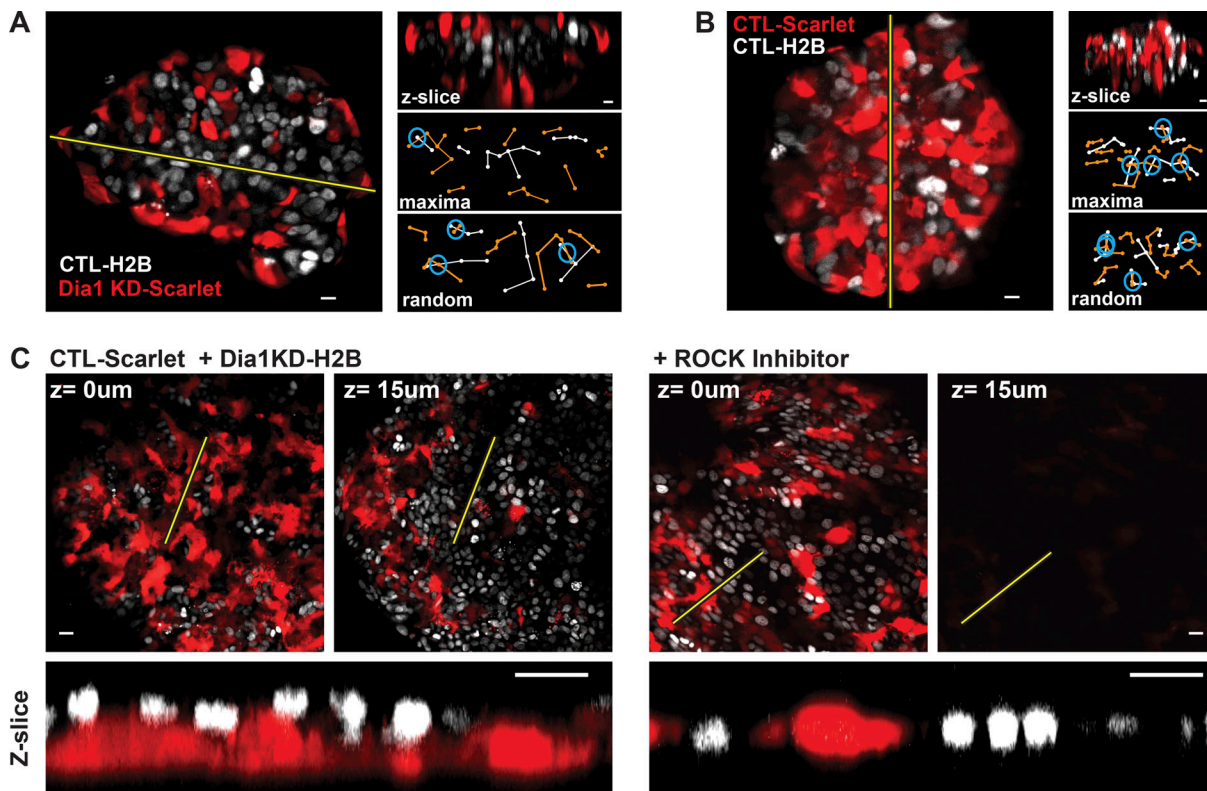


Figure 6. Differential *Dia1* expression drives ROCK-dependent separation into multiple layers. (A) Representative image of a cell aggregate formed within a hanging drop containing CTL-H2B and *Dia1KD*-Scarlet cells. Right panels: Z-slice taken along line in left panel and the networks drawn among scarlet (orange) and h2b (white) cells connecting local maxima with nearest neighbors. Includes an example of randomized maxima. Blue circles indicate network intersections. (B) Control cell aggregate experiment in which two differentially labeled populations of control cells (CTL-Scarlet and CTL-H2B) were mixed and allowed to form aggregates in suspension. Right panel shows cross section of aggregate taken along yellow line and example intersection analysis as in A. (C) Larger, 20,000 cell aggregates formed with CTL-Scarlet and *Dia1KD*-H2B (note reversal of labeling compared to A, with or without 10 μ M ROCK inhibitor. Scale bars: 10 μ m in A and B and 20 μ m in C.

recession of the *Dia1KD*-Scarlet neighbor. Conversely, in the absence of differential *Dia1* expression, intrusions made by CTL-Scarlet neighbors could become stable, possibly leading to neighbor exchange or stratification. Measuring the frequency with which intruding cells occupied a position between daughter cells as a function of time post-anaphase supported these predictions (Fig. 7 D). Measurement of intrusions made within the first hour after anaphase and tracked up to 160 min post-anaphase revealed that *Dia1* expression favored production of long-lasting intrusions (Fig. 7 E). Roughly 60% of intrusions produced by CTL-Scarlet cells lasted >80 min. Intrusions produced by *Dia1KD*-Scarlet cells, in contrast, only exceeded 80 min in 25% of attacks made upon *Dia1KD*-H2B neighbors and ~35% of those made upon CTL-H2B divisions. Thus, juxtaposition of *Dia1*-positive and negative cells enhanced the probability of *Dia1*-positive daughter cells re-integrating after division. In an *in vivo* context, these behaviors would favor channeling proliferative output into packing the basal layer.

Early in development, when keratinocytes exist as a monolayer, cells often divide in an out-of-plane, oblique manner to begin building stratified structures (Box et al., 2019). In our *in vitro* division analysis, we noted that intrusions aimed initially at the cytokinetic furrow would often expand across one of

the daughter nuclei when observed via maximum projections (see Fig. 7 C, CTL/CTL panels). This suggested that intrusions were either expanding underneath or spreading atop the daughter cell. To clarify the position of intrusions, orthogonal images were created from confocal z-slices sectioned perpendicular to the division plane (Fig. 7 F). At 2 h post-anaphase, in CTL-H2B/CTL-Scarlet mixtures, 15% of all divisions analyzed resulted in a Scarlet-labeled neighbor expanding over an H2B-marked daughter cell. A roughly equivalent number of divisions (20%) resulted in the Scarlet-labeled cell positioned beneath the daughter, in effect, an oblique division. However, when the neighbor was a *Dia1KD*-Scarlet cell, 32% of CTL-H2B divisions resulted in one daughter cell packing underneath a Scarlet-marked neighbor. Only 12% assumed the opposite arrangement. In *Dia1KD*-H2B/*Dia1KD*-Scarlet mixtures, no divisions resulted in daughters being packed beneath a Scarlet-labeled neighbor, whereas 16% placed a daughter on top of a neighbor. These behaviors likely account for the static observations made in Fig. 4 E concerning the position of CTL cells with respect to *Dia1KD* neighbors. The timing of *Dia1* downregulation with respect to stratification is not yet known. However, these data indicate that downregulation of *Dia1* by a basal cell would result in delamination and stratification when crowded by dividing, *Dia1*-positive neighbors.

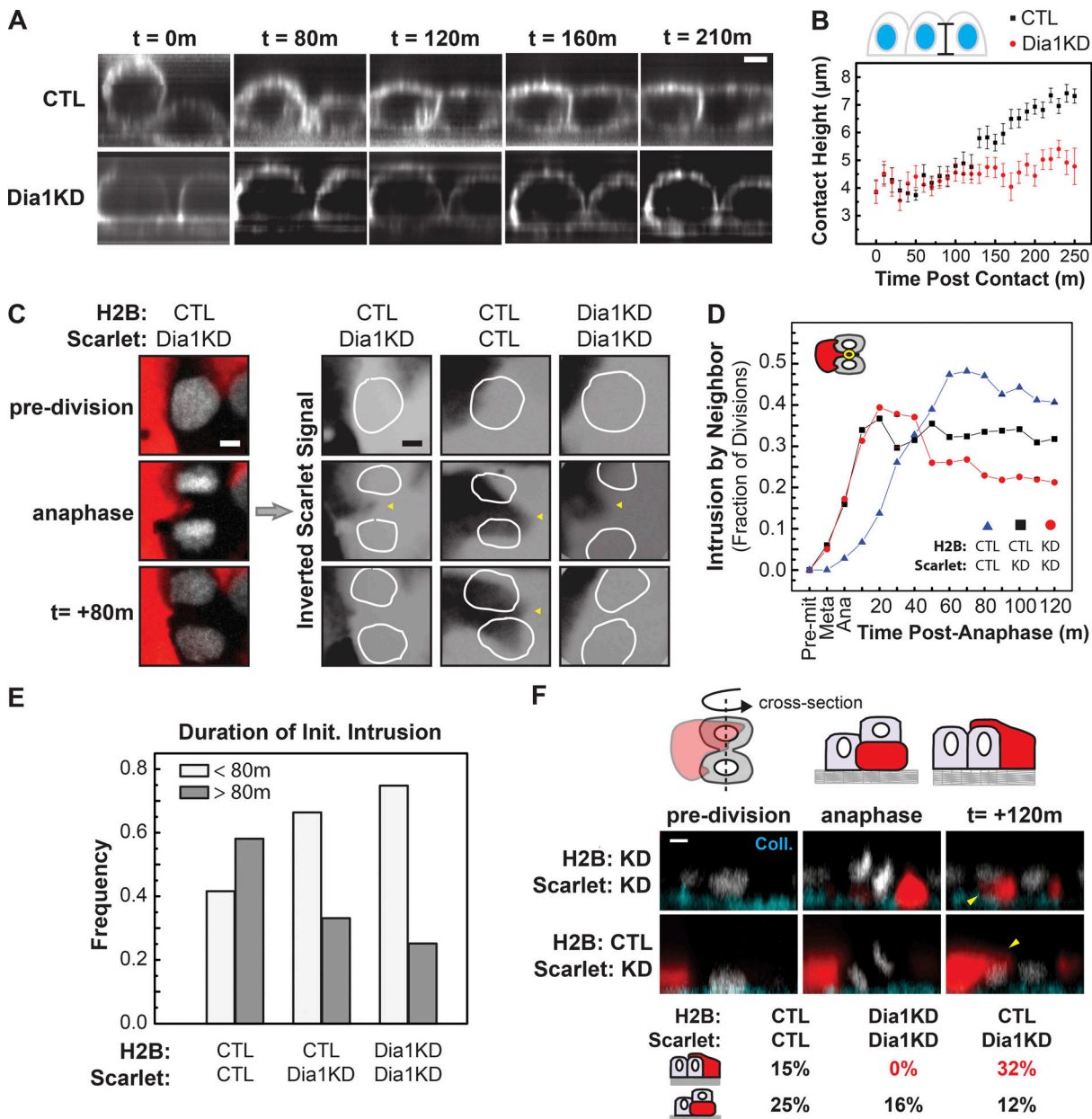


Figure 7. Dia1 expedites lateral adhesion growth and favors reintegration of dividing, Dia1 positive siblings. (A) Orthogonal view of cells labeled with siR-actin and tracked from seeding on collagen gels. 5 μ m scale bar. (B) Junction height as a function of time post-contact. A total of 20–23 junctions were analyzed per condition, mean \pm SEM. (C) Mixed culture demonstrating response of Dia1KD-Scarlet cells to a neighboring CTL-H2B cell division progressing from top to bottom panels. 5 μ m scale bar. Panels at right demonstrate intrusions (arrows) of Scarlet-labeled cells into dividing, H2B-labeled cells (nuclei/chromosomes outlined in white) for indicated cell mixtures. (D) Fraction of divisions in which a neighboring, Scarlet-labeled cell reaches the middle of an H2B-labeled division plane. 20–25 divisions per condition. (E) Frequency of short-lived (<80 min) and long-lived (>80 min) intrusions initiated within 60 min of anaphase (analysis ended at 160 min). (F) Behaviors observed in a vertical cross section, 2 h post-anaphase. Percentage of total divisions in which an H2B-labeled daughter cell packed under or on top of a neighboring Scarlet cell. Scarlet signal was considered basal or suprabasal with respect to H2B labeled cells if it occluded the H2B signal by >50%. 5 μ m scale bar. A two-tailed, independent Student's *t*-test of data in B indicated all differences beyond 120 min (except for *t* =140 min) were significant (*P* < 0.05).

Discussion

We show that Dia1 is required to construct a crowded basal layer which, in turn, supports differentiation of stratified epidermal tissue. In its absence, enforced crowding enables differentiation, indicating a primary role for Dia1 in determining basal layer mechanics. Epidermal tissue relegates YAP activity to undifferentiated basal cells and its inhibition by crowding elicits

differentiation (Elbediwy et al., 2016). Accordingly, the present study suggests that Dia1-dependent crowding impinges on this pathway en route to supporting differentiation (Fig. 8). We speculate that Dia1 supports crowding by controlling remodeling of cell–cell adhesions required in response to cells added by proliferation. Cells in a monolayer can accommodate an increasingly crowded environment by building taller lateral

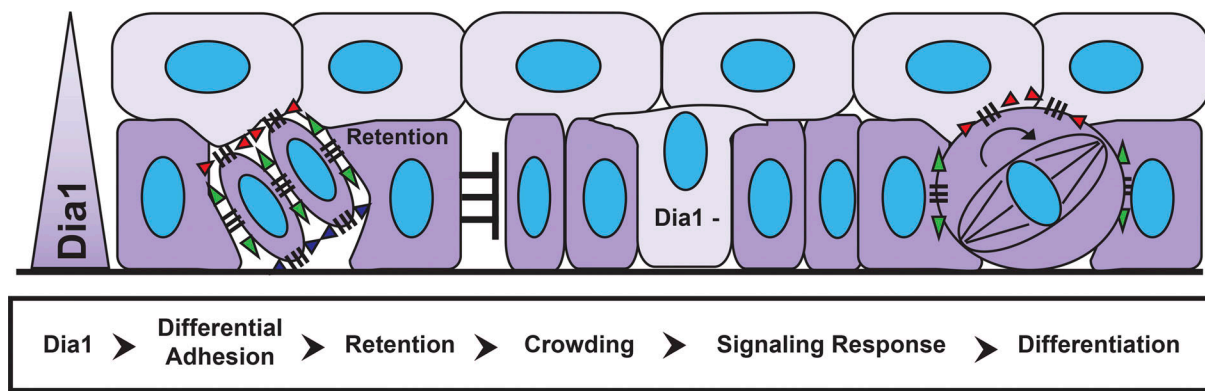


Figure 8. **Working model.** The effect of differential Dia1 expression on adhesion supports basal layer packing by favoring reintegration of dividing cells with the basal layer and preventing premature delamination.

junctions and occupying a smaller basal footprint or they can avert crowding by delaminating and leaving the monolayer entirely. Our data shows that Dia1 accelerates the growth of lateral cell–cell adhesions, which we surmise favors the option of packing cells into a crowded configuration. Accordingly, Dia1 depletion led to keratinocytes leaving the basal layer before reaching an appropriate density. This ultimately results in a stratified tissue marked by aberrant basal layer morphology and a diminished capacity for differentiation.

This work also has implications for the role of Dia1 suppression in the initiation of tissue stratification. Two dominant theories address the coupling of differentiation to cell position in stratified epithelia. Reoriented division and delamination among basal cells both contribute to populating the suprabasal compartment. However, recent intravital imaging reveals that dynamic factors pertaining to adhesion and geometry actively ensure proper execution of these processes (Box et al., 2019; Lough et al., 2019; Mesa et al., 2018; Miroshnikova et al., 2017). Though the present study did not aim to compare delamination with asymmetric division, we posit that preferential adhesions established by Dia1 expression gradients would act in both cases to channel proliferative output into basal layer packing (Fig. 8). Our data show that Dia1-negative cells interact transiently with dividing Dia1-positive cells, but these interactions fail to stabilize. In vivo, this instability would favor reintegration of dividing, Dia1-expressing cells with the basal layer, whilst driving the Dia1-suppressed cells to delaminate and form a suprabasal layer. A more resolved temporal analysis is required to determine at what timepoint inhibition of Dia1 expression, presumably by miR-198, occurs. However, this study suggests that loss of Dia1 expression among basal cells and subsequent delamination, coupled with oriented cell division, could represent a step in the stratification process. More generally, differential formin expression as a mechanism to drive differential adhesion and sorting may widely impact any epithelia in which proliferation must be shunted into populating specific compartments. Though we focused on intercellular adhesion, it should be noted that given the complex roots of cell morphology, there are likely effects stemming from cell–matrix interactions that will require further examination. Recent work, indeed, has demonstrated

that localized formin expression can alter the shaping of underlying stroma by compartments within single-layered epithelia (Sumigray et al., 2018).

Since suprabasal cells lack Dia1 but robustly resist disintegration by exogenous force, we cannot claim that Dia1 is formally required for strong intercellular adhesion in all cases. In the present work, this pointed to adhesion kinetics and cortical mechanics as the behaviors capable of driving cell segregation. Specifically, Dia1 expression accelerates expansion of a lateral contact under tension, capable of distorting the underlying collagen. We postulate that this function favors the creation of a columnar shape by expanding the lateral “wall” between two Dia1+ cells at the expense of area dedicated to the apical “roof” or basal “floor.” Thus, Dia1 may specifically populate basal cells because it uniquely provides the polymerization activity necessary to expand an adhesive surface, the lateral membrane, while under tension. Previous work has implicated cortical tension in restricting basal layer exit (Miroshnikova et al., 2017). Dia1 is a force-activated nucleator (Zimmermann and Kovar, 2019) and is implicated in cortical mechanics (Bovellan et al., 2014); these suggest particular advantages in controlling cell shape and junction remodeling during division. In the context of rearrangements elicited by basal layer divisions, expansion of lateral, Dia1-positive, homotypic junctions would outpace expansion of the apical heterotypic junction, favoring retention of cells in the basal layer. An effect on cell shape occurs both at the monolayer stage when cells lack suprabasal neighbors as well as in the presence of Dia1-negative suprabasal cells. Together, one interpretation of these results would suggest that the Dia1 expression gradient functions to mechanically isolate suprabasal cells in terms of guiding basal cell shape while maintaining adequate adhesion between the two compartments.

In summary, we have demonstrated that differential formin expression aids in defining the morphology and packing of basal layer epidermal keratinocytes with downstream impacts on differentiation. The study broaches new ground in offering evidence that specific formin expression profiles can guide cell positioning through modulating cell–cell adhesion kinetics. In addition to the implications for other formins and tissues that must channel stem cell proliferation into defined architectures,

the present study offers a unique perspective regarding the basic process of cell sorting. One implication of our work is that the adhesion kinetics associated with a formin become particularly meaningful in tissues populated by cells with heterogeneous formin expression profiles. Viewing formin expression gradients as determinants of tissue, domain architecture represents a novel perspective. Extending this possibility to the entire formin family opens a potentially fruitful avenue for exploration of morphology maintenance in all regenerative epithelia. Toward expanding upon the present work, future studies will begin tackling the potential contribution of Dial1-deficiency to *in vivo* wound healing assays, potentially in the context of skin lesions associated with myelodysplastic diseases (Keerthivasan et al., 2014; Lepelletier et al., 2019).

Materials and methods

Cell culture and reagents

The HaCaT line of immortalized keratinocytes was provided by Yu-Ying He (University of Chicago) and was originally developed by the laboratory of Norbert Fusenig (Schoop et al., 1999). HaCaTs were maintained in low calcium DMEM prepared from calcium-free DMEM powder (#09800; US Biological), spiked with 40 μ M CaCl₂, penicillin-streptomycin, L-glutamine, and 10% fetal bovine serum depleted of calcium by Chelex-100 (Sigma-Aldrich) treatment. For calcium-induced differentiation experiments, calcium concentration was raised to 2.8 mM for the indicated time span. ROCK-inhibitor (Y-27632; Cayman Chemical) was used at 10 μ M.

Antibodies and subcloning

The following antibodies were used in this study. Mouse anti-Keratin-10 (MS-611-P0; Thermo Fisher Scientific) and mouse anti-PCNA (AB29; Abcam) were used at 1:100 for immunohistochemistry. Rabbit anti-Dial1 (20624-1-AP; ProteinTech and ab129167; Abcam) was used at 1:1,000 for Western blotting and 1:100 for immunohistochemistry. Rabbit anti-GAPDH (G9545; Sigma-Aldrich) was used at 1:2,000 for Western blotting. Rabbit phospho-myosin light chain (S19; 3671; Cell Signaling) was used at 1:100 for immunostaining and 1:1,000 for Western blotting. Mouse anti-E-cadherin (ab1416; Abcam), and rabbit anti-vinculin (v4139; Sigma-Aldrich) were used at 1:100 for immunostaining.

To generate tagged mDial constructs, SnapGene software (from GSL Biotech; available at snapgene.com) was used to develop InFusion cloning (Takara) reactions for disabling the miRNA cassette and replacing the GFP in pGIPZ with mScarlet. The mScarlet insert was purchased from IDT as a gene block. Full-length mDial (NM_007858), was cloned into pGIPZ-scarlet via PCR amplification (Forward primer: 5'-GGACTCAGATCTCGAATGGAGCCGTCGGC-3' and reverse primer: 5'-TCTAGGATCCCTCGATTAGCTTGCACGGCCAACC-3') and the InFusion cloning system (Takara).

Experiments utilizing coverslip-supported collagen gels and 3D organotypic cultures

For experiments conducted on collagen gels, 75 μ l of 3.6 mg/ml rat tail collagen I (#354236; Corning) was spread upon activated

25 mm diameter coverslips. Activated coverslips were prepared by sequential incubation with 3-aminopropyltrimethoxysilane and glutaraldehyde as described in Aratyn-Schaus et al. (2010). Gel polymerization was induced by exposure to ammonium hydroxide vapor for 4 min, followed by neutralization in PBS (pH 7.4). An 8 mm (inner diameter) glass cloning ring was placed upon the center of the gel which was, subsequently, incubated overnight at 37°C in culture media prior to receiving cells. Labeling of collagen was accomplished by spiking the mixture, 1:50, with AlexaFluor-647-conjugated collagen prepared with a protein labeling kit (A20186; Thermo Fisher Scientific). Unless otherwise noted, 1.75×10^5 cells were plated per cloning ring.

Production of 3D organotypic cultures was based on protocols described by Simpson et al. (2009) with the following modifications. Collagen I solutions (ALX-522-435-0100; Enzo) of 1.5 ml (final concentration 4 mg/ml) containing J2 fibroblasts at 4.0×10^5 cells/ml were cast in 3 μ m pore filter inserts (657630; Greiner) set in deep 6-well plates (#355467; BD). Fibroblasts were allowed to condition the collagen plug overnight prior to 1.0×10^6 keratinocytes being added per collagen plug. After 2 days of submerged culture, keratinocytes were brought into contact with air by removing media from the upper chamber and allowed to stratify for the indicated duration.

Both organotypic and keratinocyte cultures grown on coverslip-supported collagen gels were carried out in E-media, based on a 3:1 DMEM:F12 media mixture supplemented with following reagents from Sigma-Aldrich: 180 μ M adenine, 5 μ g/ml insulin, 5 μ g/ml transferrin, 5 μ g/ml T3, 0.4 ng/ml hydrocortisone, 10 ng/ml cholera toxin, 4 mM L-glutamine (Sigma-Aldrich), and 10 μ g/ml gentamicin/0.25 μ g/ml amphotericin B described by Simpson et al. (2009), containing 5% fetal bovine serum. For the 2 days prior to raising to an air-liquid interface, E-media is spiked with 5 ng/ml EGF (Chemicon).

Lentiviral transduction and CRISPR editing

A pGIPZ construct carrying shRNA targeting nucleotides 1528–1546 (GGATTAATTGATCAAATGA) of the human DIAPH1 mRNA (NM_005219.4) was purchased from Dharmacon (Cat# V2LHS_43611). The Dial1 shRNA had been previously described by Bovellan et al. (2014). pGIPZ constructs were co-transfected with pHR1-8.2-deltaR and a VSV-G pseudotyping plasmid (gifts from M. Rosner) into 293T cells for lentiviral particle production via a second-generation system as described by Zufferey et al. (1997). After concentrating virus using Amicon Ultra-15 30 kD centrifugal filters, HaCaTs were incubated 6 h with concentrated virus in the presence of 4 μ g/ml polybrene. shRNA expressing cells were then selected for by incubation with puromycin. pGIPZ lentiviral transduction was also utilized for introducing Scarlet-tagged protein. GFP-H2B lentivirus were produced, similarly, but with a pLKO.1-based vector (gift from Elaine Fuchs; Addgene plasmid # 25999; <http://n2t.net/addgene:25999>; RRID: Addgene_25999). GFP-H2B transduced cells were sorted by the University of Chicago Cytometry and Antibody Technology Core.

Before conducting CRISPR editing, parental HaCaT cells were subcloned and tested to ensure that the chosen clone produced

differentiated, 3D cultures. Alt-R CRISPR-Cas9 crRNA targeting DIAPH1 exon1 (5'-UCUUCUUGUCCGGGUCCGGUUUUAGAGCUAUGCU-3') and Alt-R CRISPR-Cas9 tracrRNA ATTO-550 acquired from IDT were complexed with Cas9 enzyme (GeneArt) and transfected into a suitable HaCaT clone using Lipofectamine CRISPRMAX (Thermo Fisher Scientific) as per IDT instructions. Through flow cytometry, successfully transfected cells were identified and deposited as single cells into separate wells and allowed to expand. Successful disruption of the DIAPH1 locus in individual clones was determined by Western blot and editing at the genomic level was assessed by the CRISPR amplicon sequencing service provided by the Massachusetts General Hospital CCIB DNA Core. Specifically, a qPCR amplified portion of the DIAPH1 exon1 genomic sequence (Forward primer: 5'-CAGCGTGAACCGGACATGGA-3' and reverse primer: 5'-GACCGAGCGAAACGAGGAAGG-3') was sent for sequencing.

Western blotting and qPCR

Cell lysates were collected in Laemmli buffer and sheared with 22- and 25-gauge needles before carrying out amido black protein assays. Western blots were conducted by running equivalent amounts of protein on 4–20% Tris-Glycine SDS/polyacrylamide gradient gels (Lonza) after reduction with 2-mercaptoethanol and heating to 95°C for 5 min. Protein was transferred to nitrocellulose, overnight at 4°C in standard Tris-Glycine buffer containing 20% methanol without SDS at 30 V. Blots were blocked for 1 h in a 5% milk/0.05% Tween-20/TBS (pH 7.8) solution. Primary antibody incubation occurred overnight at 4°C in blocking buffer followed by washing with TBS/Tween and a 1 h incubation of HRP-conjugated secondary antibody at room temperature. After a final series of TBS/Tween washes, blots were developed using chemiluminescence reagent (Pierce) and film (CL-Xposure; Thermo Fisher Scientific) development. Blots for assessing shRNA-based knockdowns were done similarly; however, a LiCor Odyssey system was used to image fluorescent secondary antibodies and LiCor proprietary blocking buffers and washing instructions were used.

For qPCR, total RNA was collected using NucleoSpin kits (#740955; Macherey-Nagel). First-strand synthesis was carried out with the SuperScript III system (18080-051; Invitrogen) using an oligo dT primer and 200 ng of total RNA as input. First-strand reactions were diluted threefold, and 2 µl was used as template in 20 µl reactions containing PrimeTime master mix (1055772; IDT) and PrimeTime pre-designed qPCR primer/probe mixtures from IDT (IVL: Hs.PT.58.39460547; KRT1: Hs.PT.58.24741966; GAPDH: Hs.PT.39a.22214836). qPCR reactions were run on a StepOnePlus system (Applied Biosystems). Relative mRNA levels were calculated using the $2^{-\Delta\Delta C_t}$ method with GAPDH serving as a reference gene.

Immunohistochemistry, phalloidin and nuclei staining

Three-dimensional organotypic cultures were fixed in 10% formaldehyde for 3 days then transferred to 70% ethanol. The University of Chicago Human Tissue Resource Center paraffin-embedded, sectioned and provided hematoxylin/eosin stained slides of the skin cultures shown in Fig. 1 A, Fig. S3 D, and Fig. S5 A. This center also provided banked, paraffin-embedded

sections of human skin (Fig. S1 A) and tongue samples (Fig. S1 B). For immunohistochemistry, 5 µm sections were de-paraffinized by baking at 55°C for 1 h followed by sequential bathing in xylene and ethanol. Antigen-retrieval was conducted by holding the sections in a pH 6.0 citrate solution at 95°C for 10 min. Sections were then blocked in a 2% BSA/TBS solution and incubated with primary antibodies overnight followed by washing and incubation with secondary antibodies for 1 h. After a final series of TBS washes, sections were mounted in gelvatol.

Plucked hair follicles were isolated from the arm and processed via whole-mount immuno-staining (Fig. S1, C and D) as described by Cheng et al. (2018) and Fujiwara et al. (2011) modified so as to use TBS, rather than PBS as the buffer, and 0.5% Triton X-100, rather than Tween-20 as the detergent. Briefly, plucked hair follicles were placed in 4% paraformaldehyde/PBS for 1 h at room temperature, followed by a 1 h blocking step in 2% BSA/TBS + 0.5% Triton X-100. Primary antibody incubation occurred overnight at 4°C in blocking buffer followed by a 4-h wash in blocking buffer at room temperature. The final counterstain for nuclei and secondary antibody incubation was conducted for 3 h at room temperature in blocking buffer and utilized SPY650-DNA (Spirochrome), rather than DAPI. Following another wash, samples were mounted and imaged via confocal microscopy. The same technique, without the primary antibody incubation step, was utilized for staining nuclei of organotypic skin cultures in Fig. S4, A–C.

For staining cultured cells on coverslips, a PBS-buffered, 4% paraformaldehyde solution was applied for 10 min (20 min for cells on collagen gels). Blocking, permeabilization and quenching of paraformaldehyde was carried out by placing coverslips in a 2% BSA/TBS solution containing 0.5% Triton X-100 for 30 min. To stain nuclei and the actin cytoskeleton, coverslips were incubated with 5 µg/ml Hoechst 33342 (H3570; Thermo Fisher Scientific) and 13 nM AlexaFluor-labeled phalloidin (A12379, A12380, A22287; Thermo Fisher Scientific) in 2% BSA/TBS for 30 min at 37°C. After washing in TBS, coverslips were mounted in a Tris-buffered glycerol mountant containing N-propyl gallate.

Forced cell crowding

To conduct crowding experiments, 1 mm thick sheets of Sylgard184 (Thermo Fisher Scientific) with a 10:1 polymer to crosslinker ratio were cured at 70°C overnight. The molds created 12 mm diameter, 0.17 mm deep wells on the sheet surface. The sheets, as well as, steel washers with an inner diameter and thickness of 25 mm and 3 mm, respectively, were subjected to UV-ozone cleaning for 2 min. Washers were adhered to PDMS sheets, centered around the wells, using PDMS of a 5:1 polymer to crosslinker ratio and baked at 70°C. The 12 mm wells were biaxially stretched by clamping the washer down over a 6 mm post to increase the well area by 36% or a 4.5 mm post to acquire a 18% increase. Stretched and unstretched wells were subjected to UV-ozone cleaning followed by an overnight incubation at 4°C with 200 µg/ml collagen I in 0.017 N acetic acid. In unstretched wells, 2.13×10^5 cells were plated in low calcium media. In wells stretched to increase area by 18 and 36%, 2.50×10^5 or 2.90×10^5 cells were plated, respectively, such that all conditions received

a starting cell number of $\sim 1,900$ cells per mm^2 . Nonadherent cells were rinsed off at 1 h, and cells were incubated a further 16 h. At that point, stretched wells were released from stretch. Parallel samples were fixed immediately to check cell densities, whereas samples destined for RNA-sequencing were allowed to incubate a further 5 h prior to lysis for total RNA purification. Release of 36% prestretched PDMS caused a roughly 48% increase in cell density at the center of the well, whereas the 18% prestretched membrane resulted in a 14% increase. For induction of KRT1, cultures were allowed to incubate 9 h after stretch was released.

RNA sequencing analysis

Total RNA samples were produced as described above and submitted to the University of Chicago Genomics Facility. mRNA libraries were prepared and subjected to Illumina Hi-Seq 4000 (SR 50 bp) sequencing. MultiQC analysis indicated that samples produced between 70 and 110 million reads with 84–87% being uniquely mapped for each sample. The Illumina BaseSpace software suite was utilized to convert raw reads into transcripts per million (TPM) values for each gene. For forced crowding experiments, two independent experiments were conducted, each containing uncrowded and crowded conditions for Dial-deficient and Dial-rescue samples. After converting to fold-change over Dial-deficient values, average uncrowded, Dial-rescue values exceeding twofold (and exceeding at least 1.5-fold in each replicate) were fed into the PANTHER ontology program to produce unbiased functional annotation of Dial-induced genes. Average fold change values of Dial-rescue samples were also used in assessing the response of published gene sets pertaining to various signaling pathways. The reference sets used were as follows: suprabasal/differentiated epidermal genes (Joost et al., 2016), skin cornification diseases (Lemke et al., 2014), genes supported by the expression or activity of p63 (Truong et al., 2006), Wnt/ β -catenin (Watanabe et al., 2014), Gli/Hh (Lewandowski et al., 2015), Notch (Wang et al., 2014), SRF (Olson and Nordheim, 2010), and YAP/TAZ (Wang et al., 2018). Regarding Gli/Hh, only genes reported by Lewandowski et al. (2015) as reduced twofold by SHH knockdown with FDR < 0.05 were queried. Since a different level of crowding was reached in each experiment, the crowded/uncrowded ratios are reported separately for each experiment, rather than as averages. The enrichment of neuronal and polycomb targets among genes both reduced greater than twofold by re-expressing Dial on average and 1.25-fold upon 36% crowding was identified using GSEA software (Broad Institute).

These experiments aimed to identify early indications of differentiation and, in turn, low abundance genes were not filtered out of datasets. As such, trends within gene sets (e.g., differentiation genes, Dial-responsive genes, etc.) were deemed more meaningful than changes to individual genes. Specific genes listed in Fig. 3 are provided as examples but require more rigorous testing to achieve statistical significance.

Hanging drop aggregation assay

Cells marked with GFP-H2B and cytoplasmic mScarlet were mixed 1:1 following trypsinization, then, suspended in 20 μl

droplets of high calcium (2.8 mM) media on petri dish lids overhanging a pool of PBS. The aggregates, containing between 1.0 to 20×10^3 cells, were cultured overnight at 37°C in a cell culture incubator. Aggregates were then fixed with paraformaldehyde and transferred to a coverslip with PDMS applied to edges as a spacer. After rinsing with PBS, gelvatol was used to mount aggregates prior to imaging aggregates in a series of 0.25 μm Z-sections.

Cell doublet preparation and measurements

To produce cell doublets, cell line pairs were cocultured together at subconfluent density for 1 day, then treated with trypsin until detachment from cell culture dishes. Cells were stained with CellMask Deep Red Plasma membrane Stain (Thermo Fisher Scientific) for 10 min, then resuspended in culture medium. Around 15,000 cells in 200 μl of medium were transferred to a PDMS well, which was pretreated with 1% Pluronic f127 for 1 h then washed three times with 1X PBS. Cells were incubated in the wells at 37°C and 5% CO_2 for 4 h, then imaged at room temperature for less than 30 min. Cells were imaged by mounting PDMS wells on coverglass and using imaging methods described below. The contact angle was manually measured between isolated heterotypic pairs of cells using ImageJ.

Microscopy and live cell imaging

Confocal microscopy of fixed and live samples was conducted on an inverted microscope (Ti-E; Nikon) with a confocal scan head (CSUX; Yokogawa Electric Corporation) and laser-merge module housing 491-, 561-, and 642-nm laser lines (Spectral Applied Research), a stage controller (Prior), and a cooled CCD (HQ2-Roper Scientific) or CMOS (Zyla-Andor) camera. Images were acquired using 20×0.75 NA Plan Fluor multi-immersion, 40×1.15 NA Plan Apochromat water immersion extra-long working distance and 60×1.2 NA Plan Apochromat water immersion objectives (all from Nikon). This set up enabled capture of GFP, mScarlet, AlexaFluor 488/561/642, and SPY650 fluorophores throughout the study. Metamorph software was used for image acquisition. Live-cell imaging utilized a stage incubator for temperature, humidity, and CO_2 control (Chamlide TC and FC-5N; Quorum Technologies). The stage adapter, stage cover, and objective were maintained at 37°C, whereas humidified 5% CO_2 air was maintained at 50°C at its source to prevent condensation within its tubing. Unless otherwise noted, serial z-sections were done at 0.25- μm steps for fixed samples and 0.5- μm steps for live samples. For live, lateral membrane growth studies, cells were preincubated with 50 nM siR-actin (Cytoskeleton) for 1 h prior to trypsinization and immediate transfer to an imaging chamber. A 50 nM siR-actin concentration was maintained in the imaging media.

Image analysis and processing

ImageJ and MatLab were used for image analysis. To make basal nuclei more visible in images of living H2B-labeled 3D cultures the following filtering technique was applied to average projections of the planes spanning 10 μm up from the lowest in focus nuclear signal. The original image was modified by applying a sigma = 40 pixel median filter. The original image was

then divided by the transformed image to remove uneven background signal. For studies concerning positional relationships, H2B-labeled cells were considered to have a suprabasal neighbor if Scarlet signal from a neighbor occluded the nuclear signal by >50%. For studies utilizing only H2B-labeled cells, cells were considered suprabasal if their H2B signal occluded >50% of an underlying H2B signal or could be seen to overlie 2 or more H2B-labeled nuclei. Collagen deformation below forming junctions was taken to be the distance between the line connecting the lowest observed collagen positions between two adjacent cells and the highest position marked at forming junctions.

Measurement of cell sorting was conducted by taking serial z-slices through cell aggregates, then, reconstructing 10 orthogonal, radially configured slices per aggregate using ImageJ. Positions of local maxima for Scarlet (noise = 300 px) and GFP-H2B (noise = 60 px) signals were ascertained. MatLab was utilized to determine and connect via a line each maximum to the nearest neighbor bearing the same signal. For each cell aggregate, the number of intersections and maxima detected among the 10 slices was summed and used to calculate the average number of intersections per maxima. Matlab was used to rearrange actual maxima positions to randomized positions within the spatial constraints corresponding to each slice. Dividing the intersections per maxima value for randomized maxima by that acquired from actual observations produced, for each aggregate, a cell separation index score. Higher scores indicated less interaction between networks and a higher degree of cell sorting.

To quantify the extent to which neighboring Scarlet labeled cells invaded the space of dividing, H2B-labeled cells, the Scarlet signal was turned into a binary mask. At each timepoint after anaphase, the presence of this mask within a 5- μ m circle centered between the chromosomes of what would become two daughter cells was counted as an intrusion. The circular region of interest was centered upon premitotic and metaphase nuclei to establish a baseline level of intrusion.

Statistics

Where indicated, independent two-sample Student's *t*-tests were utilized to calculate statistical significance with *P* values <0.05 indicative of a significant difference being detected between means. Data distribution was assumed to be normal, but this was not formally tested. In cases where the sample size was small ($n \leq 6$), a nonparametric two-tailed Mann-Whitney *U* test was performed.

Online supplemental material

[Fig. S1](#) demonstrates Dial localization in human tissue samples. [Fig. S2](#) contains extra analysis of nuclear measurements taken from organotypic cultures. [Fig. S3](#) characterizes efficiency of Dial disruption techniques and additional histological images of CRISPR-edited organotypic cultures. [Fig. S4](#) contains imaging of flat-mounted organotypic cultures. [Fig. S5](#) demonstrates shRNA-mediated phenotypes in organotypic culture, presents evidence of ectopically expressed constructs, and provides additional RNAseq data. [Fig. S6](#) shows the response of SPPR genes to Dial-rescue. [Fig. S7](#) indicates the response of cell density to forced

crowding upon 18% prestretched substrates. [Fig. S8](#) has qPCR corroboration of crowding induced changes suggested by RNA-seq. [Fig. S9](#) is a duplicate experiment of the stratification time course. [Fig. S10](#) has additional data regarding proliferation, junctional actin and intercellular contact angles. [Fig. S11](#) demonstrates cell positioning effects of cultures mixed at 50:1 ratios. [Fig. S12](#) presents observations regarding division angles. [Fig. S13](#) has immunostaining images of pMLC and actin during junction development. [Fig. S14](#) demonstrates E-cadherin and vinculin staining during junction development. Tables S1, S2, S3, S4, and S5 provide separate files of the tables displayed in [Figs. 3, 4, 7, S10, and S12](#).

Acknowledgments

Thank you to Yvonne Beckham for feedback on manuscript preparation and Tracy Chmiel for scripts used in quantifying vertical cell position in [Fig. S11](#).

The above work was supported by the following funding entities: M.L. Gardel acknowledges funding from NIH ROI GM104032. RMH acknowledges funding via an NIH National Research Service Award (NIGMS:1F32GM117928-01). Christy Schmehl from University of Chicago Human Tissue Resource Center conducted histological embedding and sectioning.

The authors declare no competing financial interests.

Author contributions: R.M. Harmon conceptualized and wrote the manuscript, in addition, to devising, performing, and analyzing experiments. J. Devany aided in quantitative analysis, concept development, and manuscript preparation. M.L. Gardel aided in manuscript preparation, conceptualization, experiment planning, and data interpretation.

Submitted: 3 January 2021

Revised: 10 November 2021

Accepted: 1 March 2022

References

- Acharya, B.R., S.K. Wu, Z.Z. Lieu, R.G. Parton, S.W. Grill, A.D. Bershadsky, G.A. Gomez, and A.S. Yap. 2017. Mammalian diaphanous 1 mediates a pathway for E-cadherin to stabilize epithelial barriers through junctional contractility. *Cell Rep.* 18:2854–2867. <https://doi.org/10.1016/j.celrep.2017.02.078>
- Albanesi, C., S. Madonna, P. Gisondi, and G. Girolomoni. 2018. The interplay between keratinocytes and immune cells in the pathogenesis of psoriasis. *Front Immunol.* 9:1549. <https://doi.org/10.3389/fimmu.2018.01549>
- Aragona, M., A. Sifrim, M. Malfait, Y. Song, J. Van Herck, S. Dekoninck, S. Gargouri, G. Lapouge, B. Swedlund, C. Dubois, et al. 2020. Mechanisms of stretch-mediated skin expansion at single-cell resolution. *Nature.* 584:268–273. <https://doi.org/10.1038/s41586-020s4152555-7>
- Aratyn-Schaus, Y., P.W. Oakes, J. Stricker, S.P. Winter, and M.L. Gardel. 2010. Preparation of complaint matrices for quantifying cellular contraction. *J. Vis. Exp.* 14:2173. <https://doi.org/10.3791/2173>
- Barrandon, Y., and H. Green. 1985. Cell size as a determinant of the clone-forming ability of human keratinocytes. *Proc. Natl. Acad. Sci. USA.* 82: 5390–5394. <https://doi.org/10.1073/pnas.82.16.5390>
- Ben-Porath, I., M.W. Thomson, V.J. Carey, R. Ge, G.W. Bell, A. Regev, and R.A. Weinberg. 2008. An embryonic stem cell-like gene expression signature in poorly differentiated aggressive human tumors. *Nat. Genet.* 40: 499–507. <https://doi.org/10.1038/ng.127>
- Bovellan, M., Y. Romeo, M. Biro, A. Boden, P. Chugh, A. Yonis, M. Vaghela, M. Fritzsche, D. Moulding, R. Thorogate, et al. 2014. Cellular control of

- cortical actin nucleation. *Curr. Biol.* 24:1628–1635. <https://doi.org/10.1016/j.cub.2014.05.069>
- Box, K., B.W. Joyce, and D. Devenport. 2019. Epithelial geometry regulates spindle orientation and progenitor fate during formation of the mammalian epidermis. *Elife*. 8:e47102. <https://doi.org/10.7554/eLife.47102>
- Brakebusch, C., R. Grose, F. Quondamatteo, A. Ramirez, J.L. Jorcano, A. Pirro, M. Svensson, R. Herken, T. Sasaki, R. Timpl, et al. 2000. Skin and hair follicle integrity is crucially dependent on beta 1 integrin expression on keratinocytes. *EMBO J.* 19:3990–4003. <https://doi.org/10.1093/emboj/19.15.3990>
- Canty, L., E. Zarour, L. Kashkooli, P. Francois, and F. Fagotto. 2017. Sorting at embryonic boundaries requires high heterotypic interfacial tension. *Nat. Commun.* 8:157. <https://doi.org/10.1038/s41467-017>
- Carramusa, L., C. Ballestrem, Y. Zilberman, and A.D. Bershadsky. 2007. Mammalian diaphanous-related formin Dial controls the organization of E-cadherin-mediated cell-cell junctions. *J. Cell Sci.* 120:3870–3882. <https://doi.org/10.1242/jcs.014365>
- Carregaro, F., A.C.B. Stefanini, T. Henrique, and E.H. Tajara. 2013. Study of small proline-rich proteins (SPRRs) in health and disease: A review of the literature. *Arch. Dermatol. Res.* 305:857–866. <https://doi.org/10.1007/s00403-013-0041415-9>
- Chakraborty, S., M.N. Nagashri, S.M. Mohiyuddin, K.S. Gopinath, and A. Kumar. 2010. Gene expression profiling of oral squamous cell carcinoma by differential display rt-PCR and identification of tumor biomarkers. *Indian J. Surg. Oncol.* 1:284–293. <https://doi.org/10.1007/s13193-011s1310054-x>
- Cheng, C.C., K. Tsutsui, T. Taguchi, N. Sanzen, A. Nakagawa, K. Kakiguchi, S. Yonemura, C. Tanegashima, S.D. Keeley, H. Kiyonari, et al. 2018. Hair follicle epidermal stem cells define a niche for tactile sensation. *Elife*. 7:e38883. <https://doi.org/10.7554/eLife.38883>
- Cohen, J., S. Raviv, O. Adir, K. Padmanabhan, A. Soffer, and C. Luxenburg. 2019. The Wave complex controls epidermal morphogenesis and proliferation by suppressing Wnt-Sox9 signaling. *J. Cell Biol.* 218:1390–1406. <https://doi.org/10.1083/jcb.201807216>
- Connelly, J.T., J.E. Gautrot, B. Trappmann, D.W. Tan, G. Donati, W.T. Huck, and F.M. Watt. 2010. Actin and serum response factor transduce physical cues from the microenvironment to regulate epidermal stem cell fate decisions. *Nat. Cell Biol.* 12:711–718. <https://doi.org/10.1038/ncb2074>
- Cordenonsi, M., F. Zanconato, L. Azzolin, M. Forcato, A. Rosato, C. Frasson, M. Inui, M. Montagner, A.R. Parenti, A. Poletti, et al. 2011. The Hippo transducer TAZ confers cancer stem cell-related traits on breast cancer cells. *Cell*. 147:759–772. <https://doi.org/10.1016/j.cell.2011.09.048>
- Deyrieux, A.F., and V.G. Wilson. 2007. In vitro culture conditions to study keratinocyte differentiation using the HaCaT cell line. *Cytotechnology*. 54:77–83. <https://doi.org/10.1007/s10616-007s1069076-1>
- Elbediwy, A., Z.I. Vincent-Mistiaen, B. Spencer-Dene, R.K. Stone, S. Boeing, S.K. Wculek, J. Cordero, E.H. Tan, R. Ridgway, V.G. Brunton, et al. 2016. Integrin signalling regulates YAP and TAZ to control skin homeostasis. *Development*. 143:1674–1687. <https://doi.org/10.1242/dev.133728>
- Fagotto, F. 2014. The cellular basis of tissue separation. *Development*. 141:3303–3318. <https://doi.org/10.1242/dev.090332>
- Fiore, V.F., M. Krajnc, F.G. Quiroz, J. Levorse, H.A. Pasolli, S.Y. Shvartsman, and E. Fuchs. 2020. Mechanics of a multilayer epithelium instruct tumour architecture and function. *Nature*. 585:433–439. <https://doi.org/10.1038/s41586-020-2695-9>
- Foty, R.A., and M.S. Steinberg. 2005. The differential adhesion hypothesis: A direct evaluation. *Dev. Biol.* 278:255–263. <https://doi.org/10.1016/j.ydbio.2004.11.012>
- Fujiwara, H., M. Ferreira, G. Donati, D.K. Marciano, J.M. Linton, Y. Sato, A. Hartner, K. Sekiguchi, L.F. Reichardt, and F.M. Watt. 2011. The basement membrane of hair follicle stem cells is a muscle cell niche. *Cell*. 144:577–589. <https://doi.org/10.1016/j.cell.2011.01.014>
- Harris, A.R., A. Daeden, and G.T. Charras. 2014. Formation of adherens junctions leads to the emergence of a tissue-level tension in epithelial monolayers. *J. Cell Sci.* 127:2507–2517. <https://doi.org/10.1242/jcs.142349>
- Higashi, T., T.R. Arnold, R.E. Stephenson, K.M. Dinshaw, and A.L. Miller. 2016. Maintenance of the epithelial barrier and remodeling of cell-cell junctions during cytokinesis. *Curr. Biol.* 26:1829–1842. <https://doi.org/10.1016/j.cub.2016.05.036>
- Homem, C.C.F., and M. Peifer. 2008. Diaphanous regulates myosin and adherens junctions to control cell contractility and protrusive behavior during morphogenesis. *Development*. 135:1005–1018. <https://doi.org/10.1242/dev.016337>
- Hugh, J.M., and J.M. Weinberg. 2018. Update on the pathophysiology of psoriasis. *Cutis*. 102:6–12
- Jennemann, R., M. Rabionet, K. Gorgas, S. Epstein, A. Dalpke, U. Rothermel, A. Bayerle, F. van der Hoeven, S. Imgrund, J. Kirsch, et al. 2012. Loss of ceramide synthase 3 causes lethal skin barrier disruption. *Hum. Mol. Genet.* 21:586–608. <https://doi.org/10.1093/hmg/ddr494>
- Joost, S., A. Zeisel, T. Jacob, X. Sun, G. La Manno, P. Lonnerberg, S. Linnarsson, and M. Kasper. 2016. Single-cell transcriptomics reveals that differentiation and spatial signatures shape epidermal and hair follicle heterogeneity. *Cell Syst.* 3:221–237.e9. <https://doi.org/10.1016/j.cels.2016.08.010>
- Keerthivasan, G., Y. Mei, B. Zhao, L. Zhang, C.E. Harris, J. Gao, A.A. Basiorka, M.J. Schipma, J. McElherne, J. Yang, et al. 2014. Aberrant overexpression of CD14 on granulocytes sensitizes the innate immune response in mDial heterozygous del(5q) MDS. *Blood*. 124:780–790. <https://doi.org/10.1182/blood-2014b01-552463>
- Kobiela, A., H.A. Pasolli, and E. Fuchs. 2004. Mammalian formin-1 participates in adherens junctions and polymerization of linear actin cables. *Nat. Cell Biol.* 6:21–30. <https://doi.org/10.1038/ncb1075>
- Koehler, M.J., S. Zimmermann, S. Springer, P. Elsner, K. König, and M. Kaatz. 2011. Keratinocyte morphology of human skin evaluated by in vivo multiphoton laser tomography. *Skin Res. Technol.* 17:479–486. <https://doi.org/10.1111/j.1600-0846.2011.00522.x>
- Krens, S.F., and C.P. Heisenberg. 2011. Cell sorting in development. *Curr. Top. Dev. Biol.* 95:189–213. <https://doi.org/10.1016/B978-012-385065-2.00006-2>
- Lechler, T., and E. Fuchs. 2005. Asymmetric cell divisions promote stratification and differentiation of mammalian skin. *Nature*. 437:275–280. <https://doi.org/10.1038/nature03922>
- Lemke, J.R., K. Kernland-Lang, K. Hortnagel, and P. Itin. 2014. Monogenic human skin disorders. *Dermatology*. 229:55–64. <https://doi.org/10.1159/000362200>
- Lepelletier, C., J.D. Bouaziz, M. Rybojad, M. Bagot, S. Georgin-Lavialle, and M.D. Vignon-Pennamen. 2019. Neutrophilic dermatoses associated with myeloid malignancies. *Am. J. Clin. Dermatol.* 20:325–333. <https://doi.org/10.1007/s40257-018s4000418-2>
- Lewandowski, J.P., F. Du, S. Zhang, M.B. Powell, K.N. Falkenstein, H. Ji, and S.A. Vokes. 2015. Spatiotemporal regulation of GLI target genes in the mammalian limb bud. *Dev. Biol.* 406:92–103. <https://doi.org/10.1016/j.ydbio.2015.07.022>
- Lin, A.M., C.J. Rubin, R. Khandpur, J.Y. Wang, M. Riblett, S. Yalavarthi, E.C. Villanueva, P. Shah, M.J. Kaplan, and A.T. Bruce. 2011. Mast cells and neutrophils release IL-17 through extracellular trap formation in psoriasis. *J. Immunol.* 187:490–500. <https://doi.org/10.4049/jimmunol.1100123>
- Lough, K.J., K.M. Byrd, C.P. Descovich, D.C. Spitzer, A.J. Bergman, G.M. Beaudoin, L.F. Reichardt, and S.E. Williams. 2019. Telophase correction refines keratin orientation in stratified epithelia. *Elife*. 8:e49249. <https://doi.org/10.7554/eLife.49249>
- Luxenburg, C., E. Heller, H.A. Pasolli, S. Chai, M. Nikolova, N. Stokes, and E. Fuchs. 2015. Wdr1-mediated cell shape dynamics and cortical tension are essential for epidermal planar cell polarity. *Nat. Cell Biol.* 17:592–604. <https://doi.org/10.1038/ncb3146>
- Luxenburg, C., and R. Zaidel-Bar. 2019. From cell shape to cell fate via the cytoskeleton: Insights from the epidermis. *Exp. Cell Res.* 378:232–237. <https://doi.org/10.1016/j.yexcr.2019.03.016>
- Maitre, J.L., H. Berthoumieux, S.F. Krens, G. Salbreux, F. Julicher, E. Paluch, and C.P. Heisenberg. 2012. Adhesion functions in cell sorting by mechanically coupling the cortices of adhering cells. *Science*. 338:253–256. <https://doi.org/10.1126/science.1225399>
- Manning, M.L., R.A. Foty, M.S. Steinberg, and E.M. Schoetz. 2010. Coaction of intercellular adhesion and cortical tension specifies tissue surface tension. *Proc. Natl. Acad. Sci. USA*. 107:12517–12522. <https://doi.org/10.1073/pnas.1003743107>
- Mesa, K.R., K. Kawaguchi, K. Cockburn, D. Gonzalez, J. Boucher, T. Xin, A.M. Klein, and V. Greco. 2018. Homeostatic epidermal stem cell self-renewal is driven by local differentiation. *Cell Stem Cell*. 23:677–686.e4. <https://doi.org/10.1016/j.stem.2018.09.005>
- Miroshnikova, Y.A., H.Q. Le, D. Schneider, T. Thalheim, M. Rubsam, N. Bremicker, J. Polleux, N. Kamprad, M. Tarantola, I. Wang, et al. 2017. Adhesion forces and cortical tension couple cell proliferation and differentiation to drive epidermal stratification. *Nat. Cell Biol.* 20:69–80. <https://doi.org/10.1038/s41556-017s4150005-z>
- Moody, C.A., and L.A. Laimins. 2010. Human papillomavirus oncoproteins: Pathways to transformation. *Nat. Rev. Cancer*. 10:550–560. <https://doi.org/10.1038/nrc2886>
- Olson, E.N., and A. Nordheim. 2010. Linking actin dynamics and gene transcription to drive cellular motile functions. *Nat. Rev. Mol. Cell Biol.* 11:353–365. <https://doi.org/10.1038/nrm2890>

- Peng, J., S.M. Kitchen, R.A. West, R. Sigler, K.M. Eisenmann, and A.S. Alberts. 2007. Myeloproliferative defects following targeting of the *Drf1* gene encoding the mammalian diaphanous related formin mDial. *Cancer Res.* 67:7565–7571. <https://doi.org/10.1158/0008-5472.CAN0008-507-1467>
- Raghavan, S., C. Bauer, G. Mundschau, Q. Li, and E. Fuchs. 2000. Conditional ablation of beta1 integrin in skin. Severe defects in epidermal proliferation, basement membrane formation, and hair follicle invagination. *J. Cell Biol.* 150:1149–1160. <https://doi.org/10.1083/jcb.150.5.1149>
- Rorke, E.A., G. Adhikary, C.A. Young, R.H. Rice, P.M. Elias, D. Crumrine, J. Meyer, M. Blumenberg, and R.L. Eckert. 2015. Structural and biochemical changes underlying a keratoderma-like phenotype in mice lacking suprabasal AP1 transcription factor function. *Cell Death Dis.* 6: e1647. <https://doi.org/10.1038/cddis.2015.21>
- Schoop, V.M., N. Mirancea, and N.E. Fusenig. 1999. Epidermal organization and differentiation of HaCaT keratinocytes in organotypic coculture with human dermal fibroblasts. *J. Invest Dermatol.* 112:343–353. <https://doi.org/10.1046/j.1523-1747.1999.00524.x>
- Simpson, C.L., S. Kojima, and S. Getsios. 2009. RNA interference in keratinocytes and an organotypic model of human epidermis. *Methods Mol. Biol.* 585:127–146. https://doi.org/10.1007/978-1-60761-380-0_10
- Simpson, C.L., D.M. Patel, and K.J. Green. 2011. Deconstructing the skin: Cytoarchitectural determinants of epidermal morphogenesis. *Nat. Rev. Mol. Cell Biol.* 12:565–580. <https://doi.org/10.1038/nrm3175>
- Sumigray, K.D., M. Terwilliger, and T. Lechler. 2018. Morphogenesis and compartmentalization of the intestinal crypt. *Dev. Cell.* 45:183–197.e5. <https://doi.org/10.1016/j.devcel.2018.03.024>
- Sundaram, G.M., J.E. Common, F.E. Gopal, S. Srikanta, K. Lakshman, D.P. Lunny, T.C. Lim, V. Tanavde, E.B. Lane, and P. Sampath. 2013. ‘See-saw’ expression of microRNA-198 and FSTL1 from a single transcript in wound healing. *Nature.* 495:103–106. <https://doi.org/10.1038/nature11890>
- Sundaram, G.M., H.M. Ismail, M. Bashir, M. Muhuri, C. Vaz, S. Nama, G.S. Ow, I.A. Vladimirovna, R. Ramalingam, B. Burke, et al. 2017. EGF hijacks miR-198/FSTL1 wound-healing switch and steers a two-pronged pathway toward metastasis. *J. Exp. Med.* 214:2889–2900. <https://doi.org/10.1084/jem.20170354>
- Tinkle, C.L., H.A. Pasolli, N. Stokes, and E. Fuchs. 2008. New insights into cadherin function in epidermal sheet formation and maintenance of tissue integrity. *Proc. Natl. Acad. Sci. USA.* 105:15405–15410. <https://doi.org/10.1073/pnas.0807374105>
- Totaro, A., M. Castellan, G. Battilana, F. Zanconato, L. Azzolin, S. Giulitti, M. Cordenonsi, and S. Piccolo. 2017. YAP/TAZ link cell mechanics to Notch signalling to control epidermal stem cell fate. *Nat. Commun.* 8:15206. <https://doi.org/10.1038/ncomms15206>
- Truong, A.B., M. Kretz, T.W. Ridky, R. Kimmel, and P.A. Khavari. 2006. p63 regulates proliferation and differentiation of developmentally mature keratinocytes. *Genes Dev.* 20:3185–3197. <https://doi.org/10.1101/gad.1463206>
- van der Kammen, R., J.Y. Song, I. de Rink, H. Janssen, S. Madonna, C. Scarponi, C. Albanesi, W. Brugman, and M. Innocenti. 2017. Knockout of the Arp2/3 complex in epidermis causes a psoriasis-like disease hallmarked by hyperactivation of transcription factor Nrf2. *Development.* 144: 4588–4603. <https://doi.org/10.1242/dev.156323>
- Vasioukhin, V., C. Bauer, L. Degenstein, B. Wise, and E. Fuchs. 2001. Hyperproliferation and defects in epithelial polarity upon conditional ablation of alpha-catenin in skin. *Cell.* 104:605–617. [https://doi.org/10.1016/S0092-8674\(01\)00246-x](https://doi.org/10.1016/S0092-8674(01)00246-x)
- Wang, G.Q., C.C. Abnet, Q. Shen, K.J. Lewin, X.D. Sun, M.J. Roth, Y.L. Qiao, S.D. Mark, Z.W. Dong, P.R. Taylor, and S.M. Dawsey. 2005. Histological precursors of oesophageal squamous cell carcinoma: Results from a 13 year prospective follow up study in a high risk population. *Gut.* 54: 187–192. <https://doi.org/10.1136/gut.2004.046631>
- Wang, H., C. Zang, L. Taing, K.L. Arnett, Y.J. Wong, W.S. Pear, S.C. Blacklow, X.S. Liu, and J.C. Aster. 2014. NOTCH1-RBP complexes drive target gene expression through dynamic interactions with superenhancers. *Proc. Natl. Acad. Sci. USA.* 111:705–710. <https://doi.org/10.1073/pnas.1315023111>
- Wang, Y., X. Xu, D. Maglic, M.T. Dill, K. Mojumdar, P.K. Ng, K.J. Jeong, Y.H. Tsang, D. Moreno, V.H. Bhavana, et al. 2018. Comprehensive molecular characterization of the hippo signaling pathway in cancer. *Cell Rep.* 25: 1304–1317.e5. <https://doi.org/10.1016/j.celrep.2018.10.001>
- Watanabe, K., J. Biesinger, M.L. Salmans, B.S. Roberts, W.T. Arthur, M. Cleary, B. Andersen, X. Xie, and X. Dai. 2014. Integrative ChIP-seq/microarray analysis identifies a CTNBN1 target signature enriched in intestinal stem cells and colon cancer. *PLoS One.* 9:e92317. <https://doi.org/10.1371/journal.pone.0092317>
- Watt, F.M. 1984. Selective migration of terminally differentiating cells from the basal layer of cultured human epidermis. *J. Cell Biol.* 98:16–21. <https://doi.org/10.1083/jcb.98.1.16>
- Whitson, R.J., A. Lee, N.M. Urman, A. Mirza, C.Y. Yao, A.S. Brown, J.R. Li, G. Shankar, M.A. Fry, S.X. Atwood, et al. 2018. Noncanonical hedgehog pathway activation through SRF-MKL1 promotes drug resistance in basal cell carcinomas. *Nat. Med.* 24:271–281. <https://doi.org/10.1038/nm.4476>
- Xing, J., and C. Liu. 2017. Identification of genes associated with histologic tumor grade of esophageal squamous cell carcinoma. *FEBS Open Bio.* 7: 1246–1257. <https://doi.org/10.1002/2211-5463.12228>
- Yang, J., L. Zhou, Y. Zhang, J. Zheng, J. Zhou, Z. Wei, and J. Zou. 2019. DIAPH1 is upregulated and inhibits cell apoptosis through ATR/p53/Caspase-3 signaling pathway in laryngeal squamous cell carcinoma. *Dis. Markers.* 2019:6716472. <https://doi.org/10.1155/2019/6716472>
- Zhou, K., A. Muroyama, J. Underwood, R. Lylek, S. Ray, S.H. Soderling, and T. Lechler. 2013. Actin-related protein2/3 complex regulates tight junctions and terminal differentiation to promote epidermal barrier formation. *Proc. Natl. Acad. Sci. USA.* 110:E3820–E3829. <https://doi.org/10.1073/pnas.1308419110>
- Zimmermann, D., and D.R. Kovar. 2019. Feeling the force: Formin’s role in mechanotransduction. *Curr. Opin. Cell Biol.* 56:130–140. <https://doi.org/10.1016/j.celb.2018.12.008>
- Zufferey, R., D. Nagy, R.J. Mandel, L. Naldini, and D. Trono. 1997. Multiply attenuated lentiviral vector achieves efficient gene delivery in vivo. *Nat. Biotechnol.* 15:871–875. <https://doi.org/10.1038/nbt0997-871>

Supplemental material

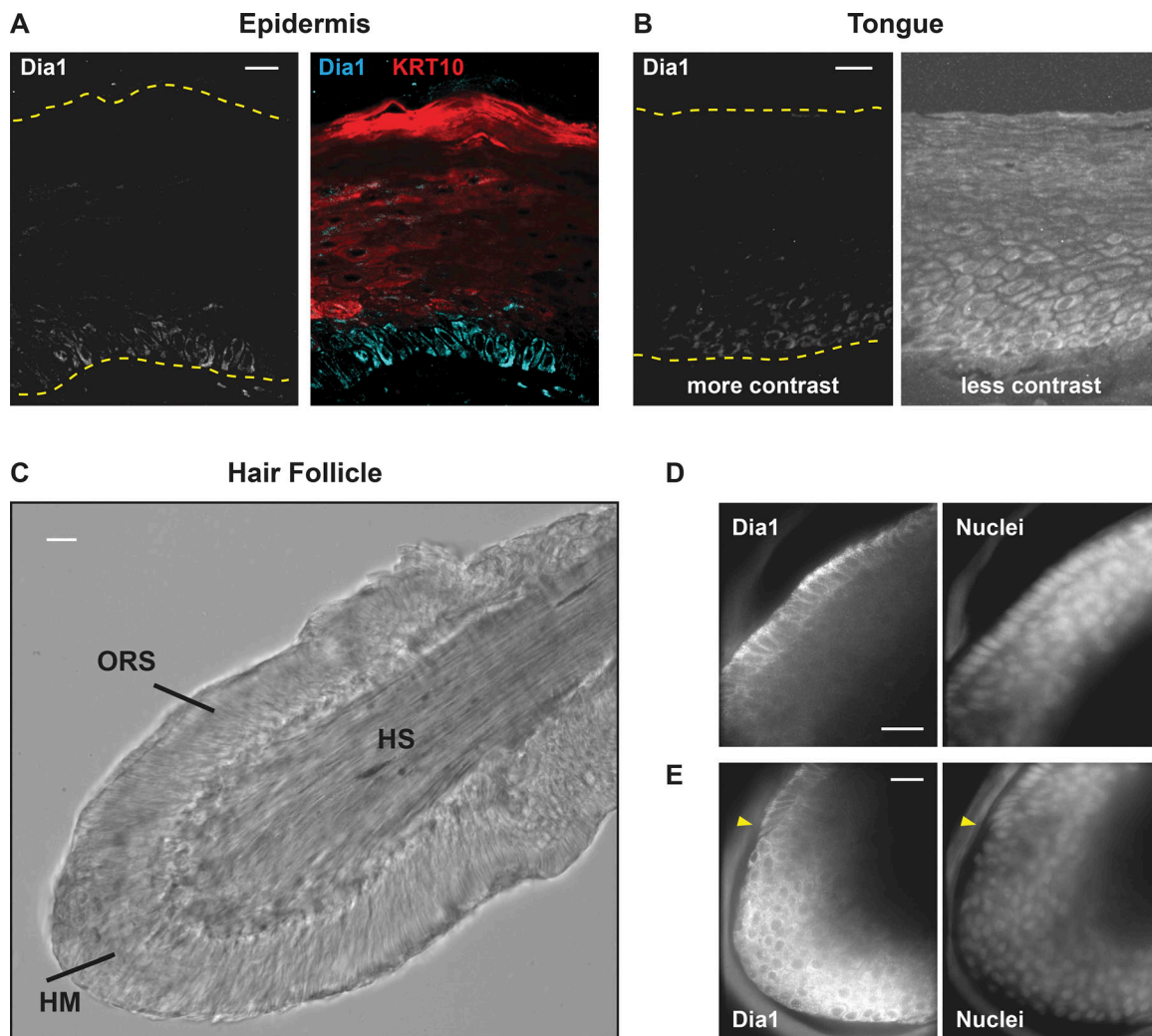


Figure S1. **Dia1 in human stratified epithelia.** **(A)** Dia1 and KRT10 staining in a human epidermal tissue section. Yellow dashed lines approximate lower and upper boundaries of the keratinocyte compartment. **(B)** Dia1 staining in a tissue section of the tongue surface. Yellow lines approximate upper and lower boundaries of the keratinocyte compartment. **(C)** Low magnification phase image of a plucked, human hair follicle in the bulb region. Approximate locations of the outer root sheath (ORS), the hair matrix cells (HM) and the hair shaft (HS) indicated. **(D)** Higher magnification image of the ORS region stained for Dia1 and nuclei. A 1-pixel Gaussian blur was applied to the nuclear images. **(E)** Dia1 and nuclei staining of the hair matrix region. Note the transition of Dia1 staining distribution at the site of transition between HM and the more columnar cells of the ORS (yellow arrow). Halo surrounding fluorescence images is assumed to be background from dermal tissue removed during plucking. Scale bars = 20 μ m.

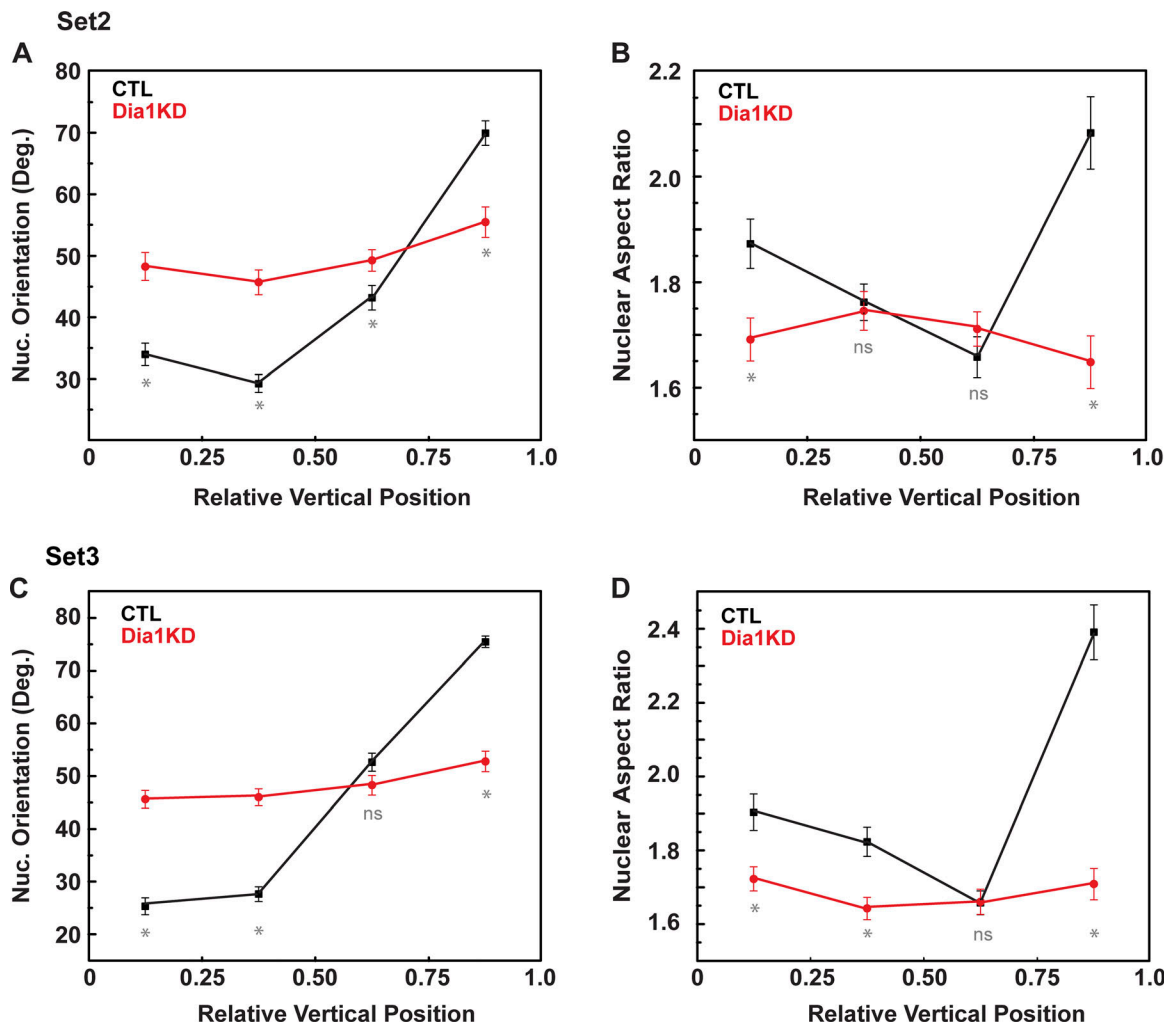


Figure S2. **Nuclear orientation and aspect ratios for two additional datasets.** Corresponds to Fig. 1, D and E. **(A and B)** Dataset2 nuclear orientations and aspect ratios with respect to relative vertical height in the tissue. Datapoints represent mean \pm SEM derived from 82 to 236 nuclei lying within bins bounded by x-axis ticks. **(C and D)** Dataset3 nuclear orientations and aspect ratios with respect to relative vertical height in the tissue. Datapoints represent mean \pm SEM derived from 118 to 246 nuclei lying within bins bounded by x-axis ticks. Independent, two-tailed Student's t-test results are indicated as: $P < 0.05$ (*); $P > 0.05$ was considered not significant (ns).

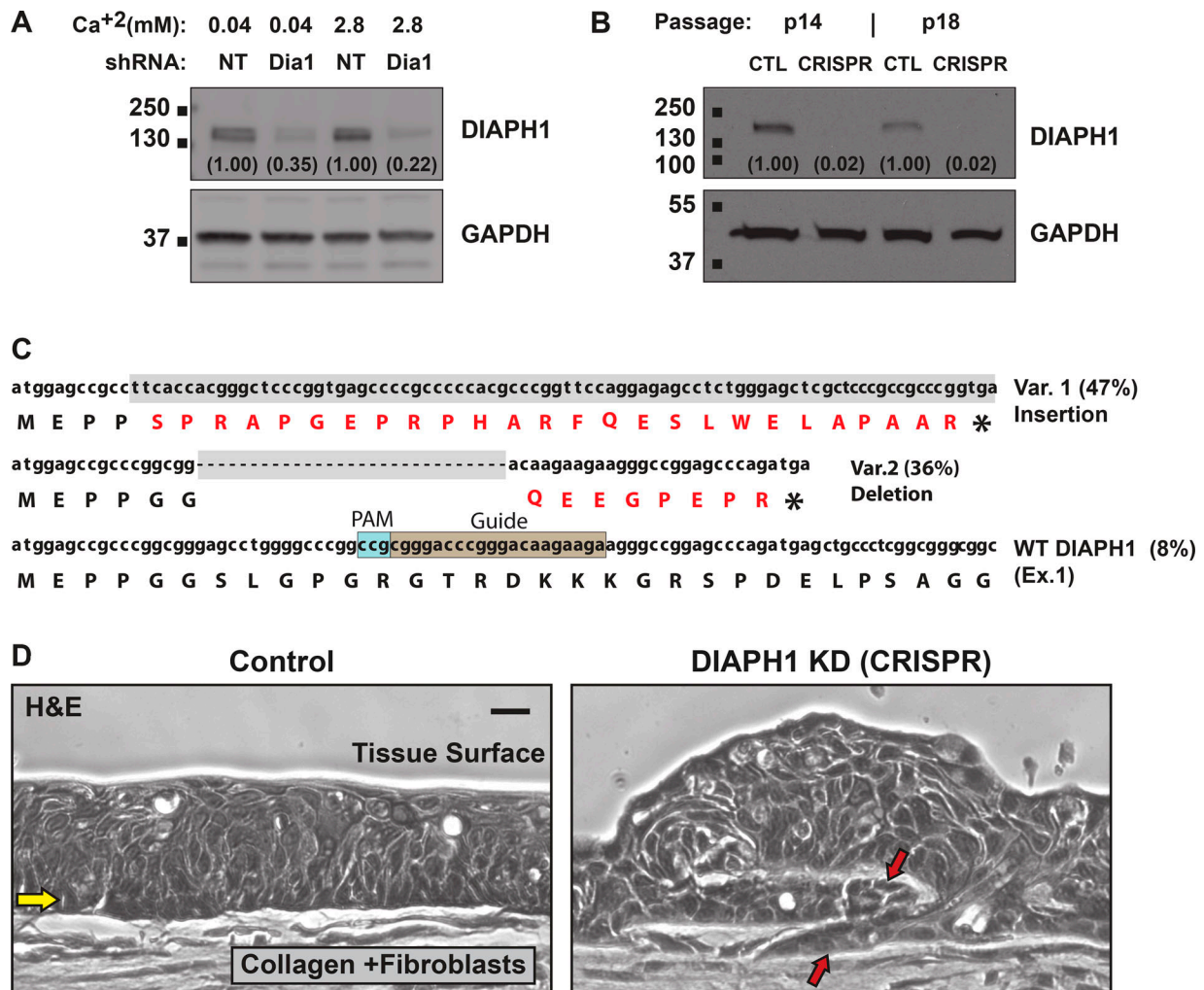


Figure S3. **Disruption of DIAPH1 gene expression and example of ingressions found in DIAPH1-deficient cultures.** (A) Western blot analysis of HaCaT cells transduced with nontargeting (NT) and DIAPH1-directed (Dia1) shRNA via lentivirus, cultured in low or high calcium media for 20 h. Relative abundance indicated with respect to control samples. Black squares = molecular weight markers at indicated weight (in kilodaltons). (B) Western blot analysis of control cells (CTL) and those carrying a disrupted DIAPH1 locus (CRISPR) at two different passages. Relative abundance to controls is indicated. (C) NGS analysis of genomic DNA flanking CRISPR-editing site and variant frequency. (D) Example of DIAPH1-deficient tissue growth into the underlying collagen substrate. Hematoxylin and eosin stain of cross sectioned, paraffin-embedded tissue fixed 10 days after raising to an air-liquid interface. Scale bar = 20 μ m. Yellow arrow indicates basal keratinocyte layer. Red arrows indicate distinct ingressions.

Downloaded from http://rupress.org/jcb/article-pdf/221/5/e202101008/1430385/jcb_202101008.pdf by Univ Chicago Science Lib user on 24 March 2022

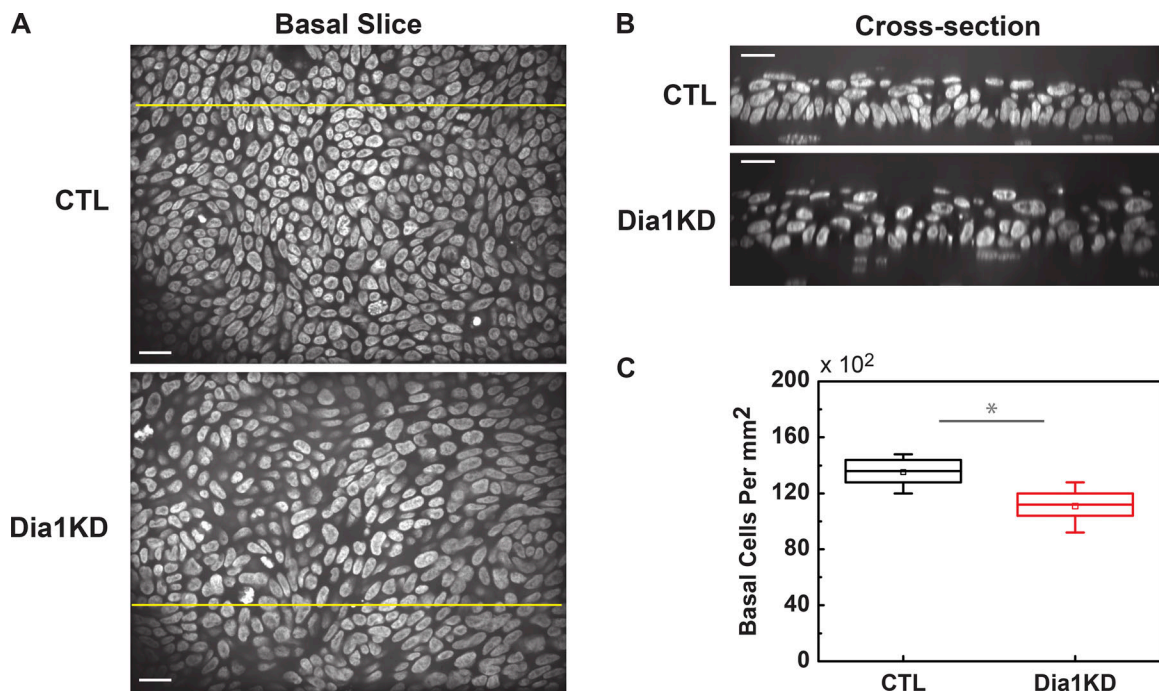


Figure S4. **Flat-mounted imaging of 3D organotypic cultures.** Pertains to Fig. 1. **(A)** CTL and Dia1KD organotypic cultures were stained for nuclei, flat mounted, and imaged at the most basal in-focus plane. **(B)** Orthogonal slices corresponding to the positions marked by yellow lines in A. **(C)** Measurement of cell density in the basal plane. 31, 50 × 50 μm fields were sampled from cultures imaged via confocal z-slices. Basal nuclei in averaged projections from the bottom 6 μm were counted. Boxes = 25–75 percentile, whiskers 10–90 percentile, square = mean, line = median. Two-tailed, independent Student t-test values of $P < 0.05$ are indicated with an asterisk. Scale bars = 20 μm.

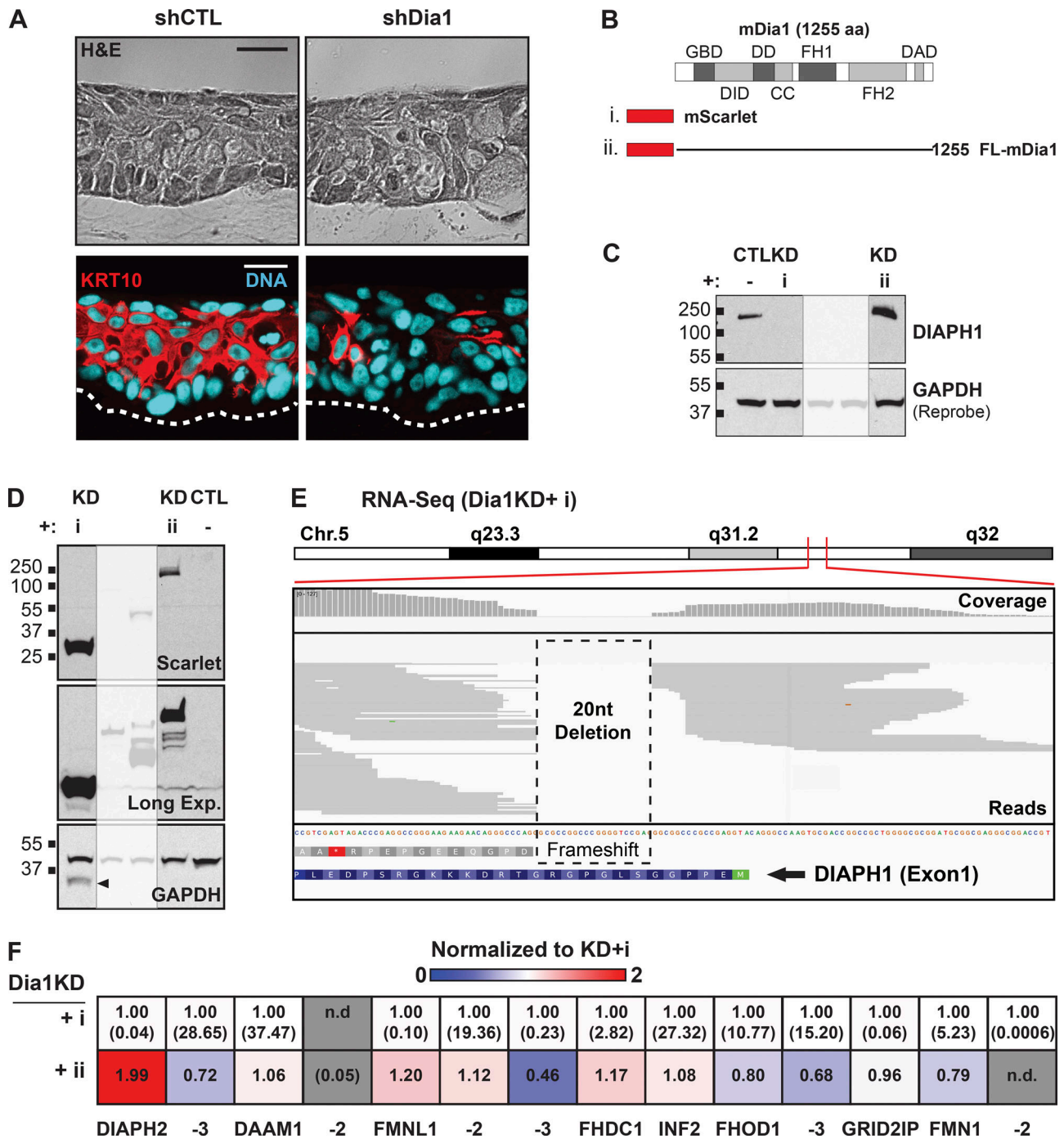


Figure S5. **Organotypic cultures treated with shRNA, ectopic mDia1 constructs, and ancillary RNA-seq data.** (A) Hematoxylin and eosin (H&E) staining and keratin-10 (KRT10) staining of organotypic cultures transduced with control or Dia1-targeted shRNA. Counterstained with Hoechst for DNA. Dotted line indicates keratinocyte/collagen boundary. Scale bars = 20 μ m. (B) Map of mDia1 construct introduced to CRISPR-edited Dia1 knockdown (Dia1KD) cells via lentivirus. Numerals are referenced in subsequent panels. FL = full length. (C and D) Western blot analysis of ectopic constructs blotted with anti-DIAPH1 (C) or anti-Cherry (D). Residual Scarlet signal indicated by arrowhead. Irrelevant lanes of Western blot lanes were dimmed for clarity. Black squares = molecular weight markers at indicated weight (in kilodaltons). (E) RNA-seq analysis of DIAPH1 transcripts in CRISPR-edited Dia1KD cells. All detected transcripts contained deletions in the first exon. (F) RNA-seq derived quantities of other mammalian formin genes. Values in parentheses represent average transcripts per million (tpm) value in Dia1KD cells from two experiments. Levels in Dia1-rescue cells (ii) were normalized to this value and are indicated in the heatmap. DAAM2 was not detected in Dia1KD cells, thus, the average tpm for rescue cells is given.

Downloaded from http://rupress.org/jcb/article-pdf/221/5/e202101008/1430385/jcb_202101008.pdf by Univ Chicago Science Lib user on 24 March 2022

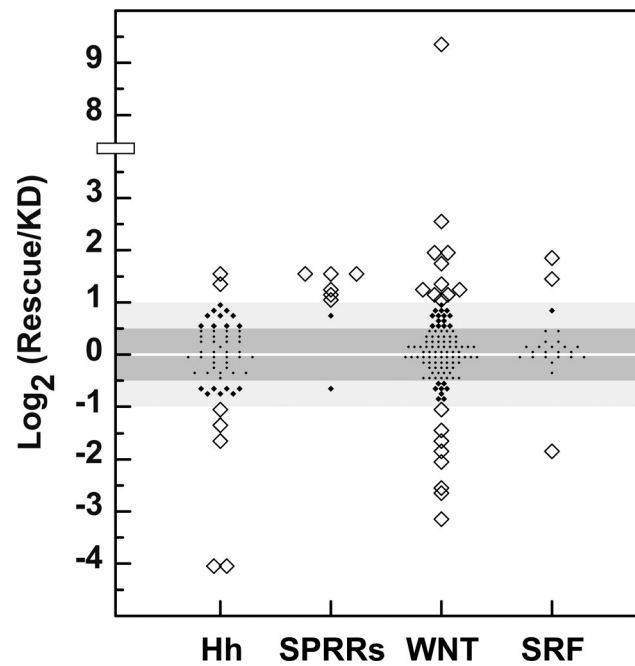


Figure S6. **Response of known gene sets to re-expression of Dia1.** RNA sequencing results tracking the expression of transcripts known to be upregulated by the indicated signaling pathways, comparing Dia1-rescue cells relative to Dia1KD-Scarlet counterparts. Studies identifying the plotted gene sets are listed in the Methods section. SPRR (small proline rich repeat proteins) are known markers of keratinocyte differentiation. All SPRR genes listed in the NCBI Gene database with nonzero expression values in both the Dia1-deficient and Dia1-rescue lines are plotted. Data represent the average fold-change value of individual genes derived from two independent experiments, corresponding to the uncrowded conditions described in Fig. 3. Average values were converted to Log_2 form for presentation.

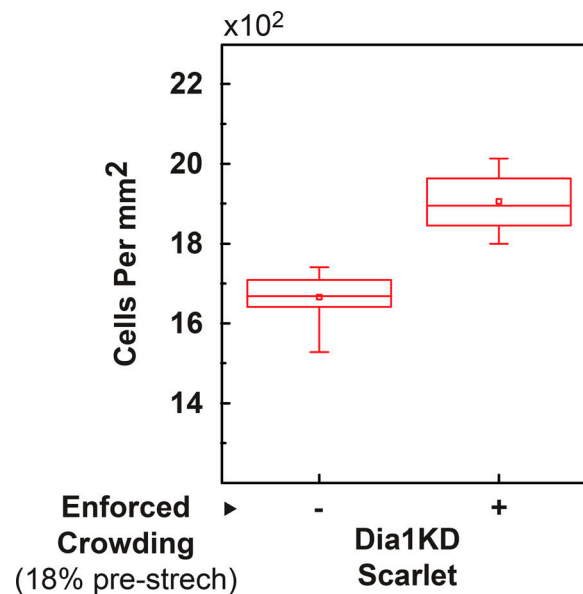


Figure S7. **Cell density response to relaxing an 18% prestretched PDMS substrate.** Crowding quantified in terms of cell density with and without forced crowding. 18 fields per condition. Box plots = 25–75 percentile, whiskers = 10–90th percentile, line = median, square = mean.

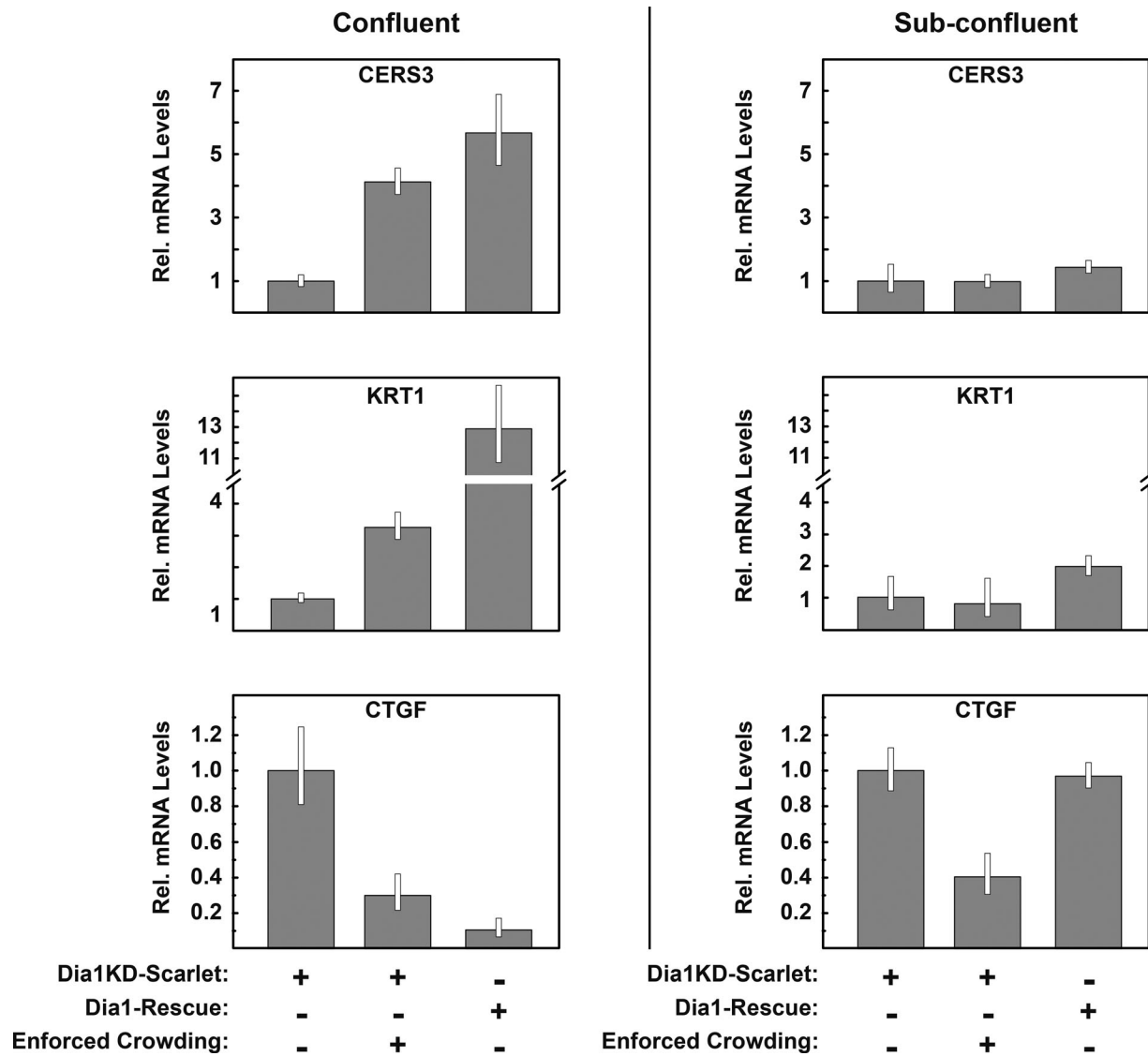


Figure S8. **Corroboration of RNAseq-enforced crowding results By qPCR.** RNA samples of cells plated on prestretched PDMS (36%) were collected 9 h after relaxing substrates and subjected to qPCR. The differentiation markers CERS3 and KRT1 were assessed as representatives of Dia1-induced genes and CTGF was assessed as a representative of genes repressed by Dia1 expression. Panels on the right are of experiments conducted similarly but with 1/4 the number of cells plated. Results represent mRNA expression relative to levels determined for Dia1KD-Scarlet samples without enforced crowding. White boxes indicate the 95% CI of three, technical replicates from one experiment. Columns = mean of those three replicates.

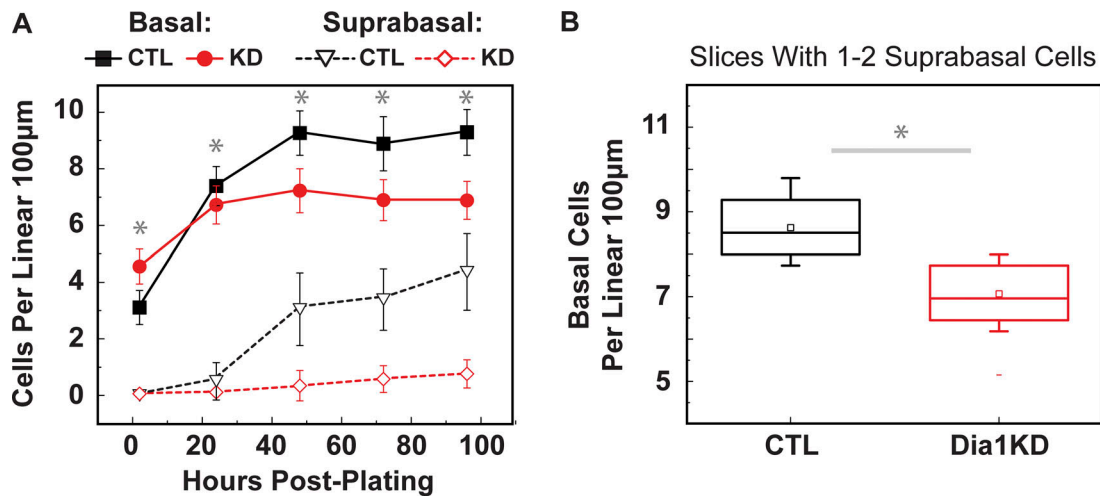


Figure S9. **Duplicate stratification time course.** Pertains to Fig. 4, B and C. **(A)** Counting of basal and suprabasal cells per orthogonal slice with respect to time since plating. 84–126 orthogonal slices per condition per timepoint were analyzed. H2B signals occluding >50% of an underlying H2B signal or overlying multiple H2B-labeled nuclei were considered suprabasal. Plotted values represent the mean \pm SEM per slice. **(B)** Linear density of basal cells in z-slices, limited to slices containing only 1–2 suprabasal cells per 100µm, regardless of timepoint. Data represents cell number per slice (CTL: 46 slices, Dia1KD: 78 slices). Boxes = 25–75th percentile, whiskers = 10–90th percentile, square = mean, line = median. Two-tailed, independent Student’s *t*-test results are indicated, where $P < 0.05$ (*). In A, *t* tests were conducted on basal cell density values.

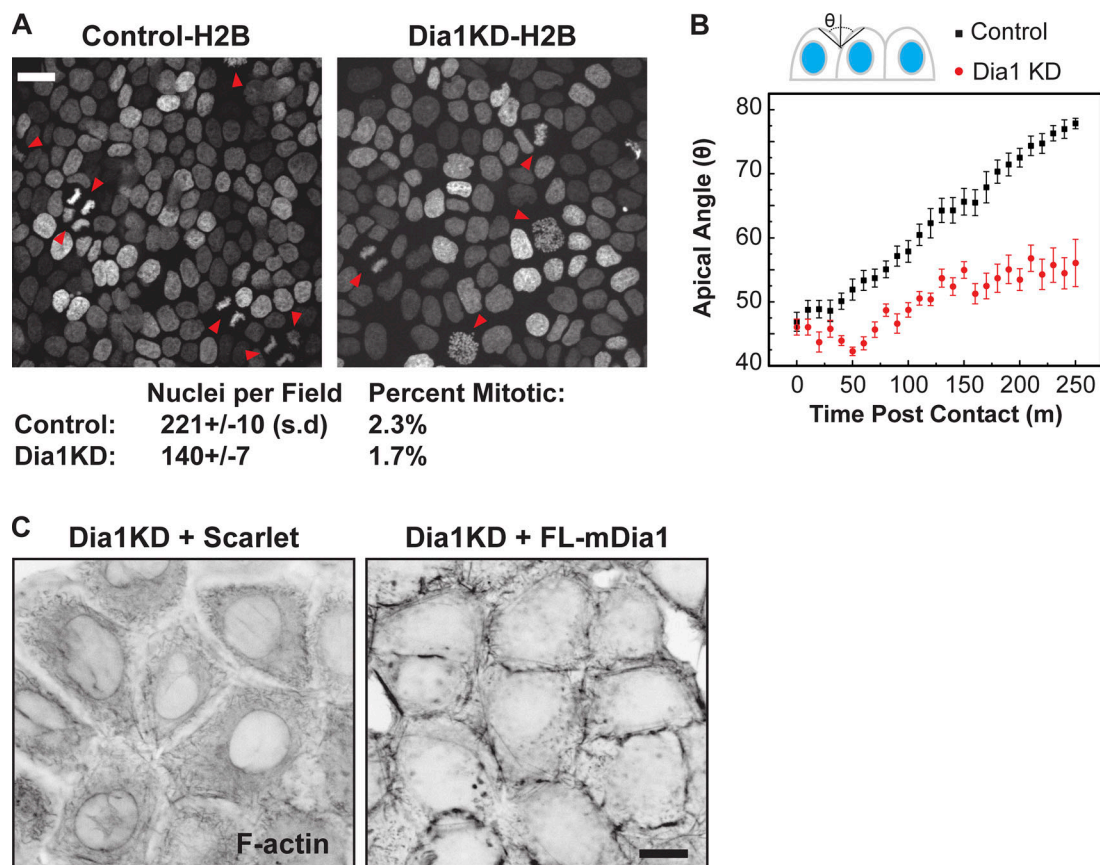


Figure S10. **Effects of Dia1 expression on proliferation, intercellular contact angles, and junctional actin.** **(A)** Hoechst stained nuclei 24 h post-plating on collagen gels. Arrowheads mark mitotic cells. Mean cell density per field \pm SD (CTL: 5 fields, Dia1KD: 8 fields) is indicated. Percent of nuclei with mitotic morphology was determined from 1,131 to 1,136 CTL and Dia1KD cells, respectively. SD = standard deviation. Field = 27,500 μm^2 . **(B)** Angle formed between cell apices and the top of developing intercellular junctions labeled via siR-actin and imaged live after contact initiation Angle is divided by two to comply with contact angle conventions. About 20–22 junctions analyzed per condition. Datapoints represent the mean \pm SEM at each time point. **(C)** Phalloidin staining of F-actin in fixed Dia1KD and Dia1-Rescue cells 1 h after plating on collagen gels, imaged 2.5 μm above the substrate. Scale bars = 20 μm for A, 10 μm for C. Box plots = 25–75th percentile, line = median, square = mean, whiskers = 5–95th percentile and circles mark measurements for individual cells.

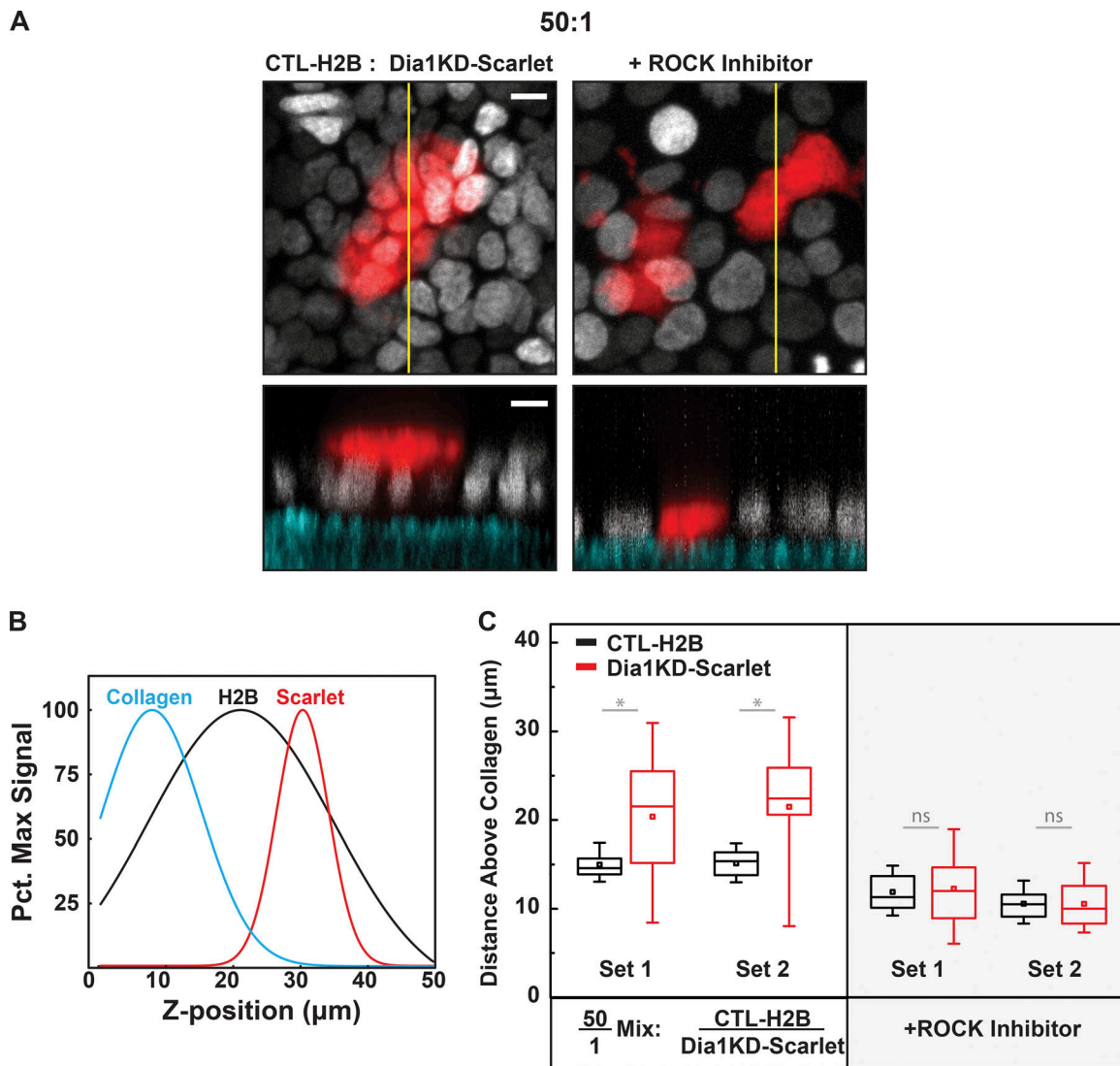


Figure S11. **Effect of differential Dia1 expression on cell position in 50:1 mixed cultures.** (A) Maximum projections and orthogonal slices taken along the yellow lines (lower panels) demonstrating the arrangement of H2B and Scarlet marked cells of differing Dia1 expression with respect to the underlying collagen gel (cyan). Mixtures of the indicated cell types were prepared at 50:1 ratios with or without 10 μ M ROCK inhibitor and imaged 48 h post-plating. Scale bar = 10 μ m. (B) Example z-plot profile of an 80 \times 80 μ m field encompassing a small colony of Dia1KD-Scarlet cells embedded in CTL-H2B cells. (C) Quantitation of Scarlet labeled cell positions with respect to collagen determined by z-plot profiles of 56 (Set1), 36 (Set2), 40 (ROCK Inhibited, Set1), and 49 (ROCK Inhibited, Set2) 80 \times 80 μ m fields encompassing single cells or small colonies of Scarlet-marked cells. Box plots: 25–75th percentile, whiskers = 10–90th percentile, small square = mean. Two-tailed, independent Student's *t*-test values $P < 0.05$ are marked with an asterisk.

Downloaded from http://rupress.org/jcb/article-pdf/221/5/e202101008/1430385/jcb_202101008.pdf by Univ Chicago Science Lib user on 24 March 2022

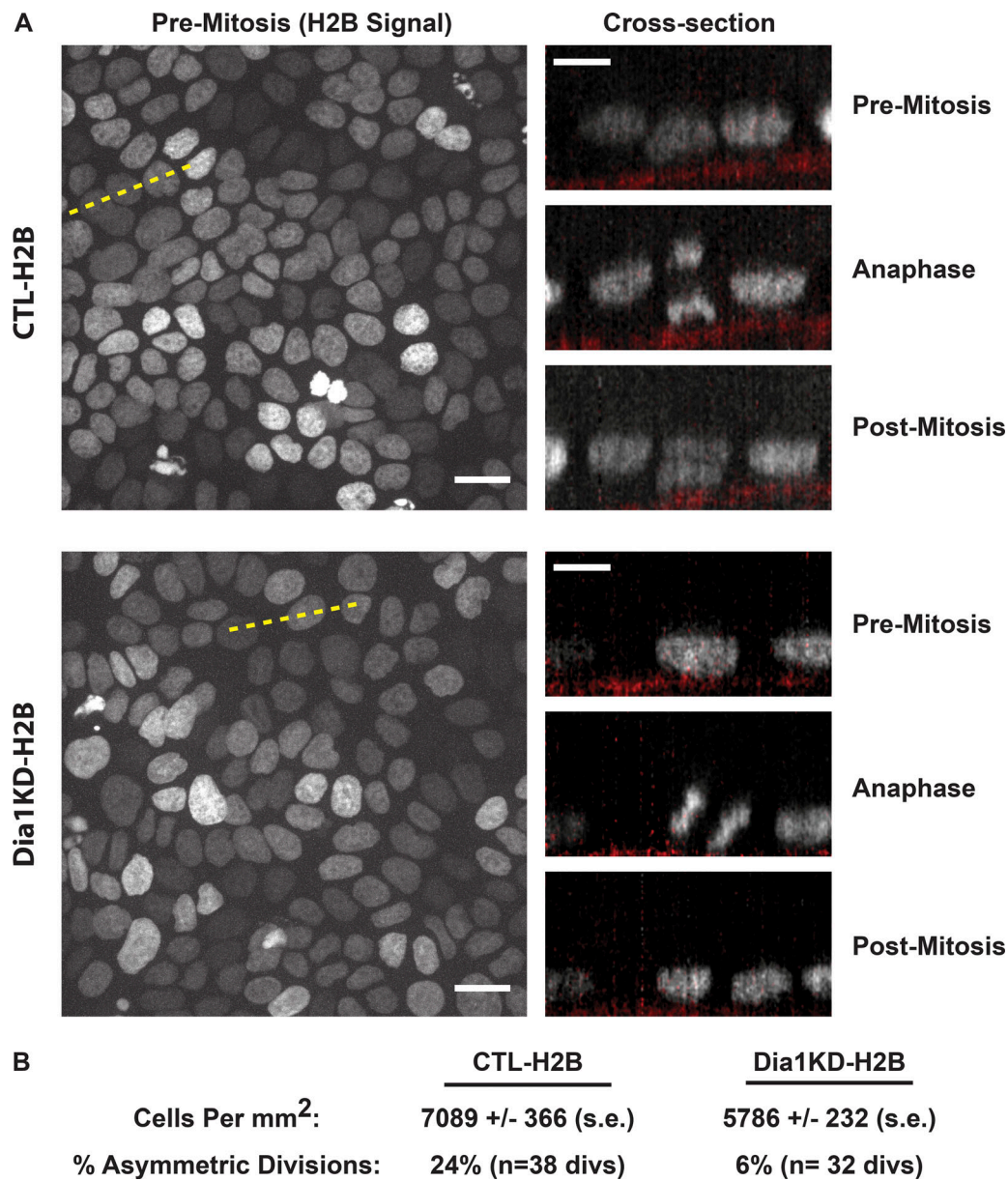


Figure S12 **Effect of Dia1 expression on division orientation.** (A) Left panels: H2B labeled cells imaged at the beginning of a live cell imaging experiment. Right panels: Cross sections taken from the cells marked by the yellow dashed lines over time pre-mitosis, during anaphase and post-anaphase. (B) Mean cell densities \pm SEM determined from five separate fields at the beginning of the live imaging experiment. The percentage of cell divisions (CTL: 38 divisions, Dia1KD: 32 divisions) observed to divide asymmetrically. Scale bars = 20 μ m (main panels) and 10 μ m (cross-section panels).

Downloaded from http://rupress.org/jcb/article-pdf/221/5/e202101008/1430385/jcb_202101008.pdf by Univ Chicago Science Lib user on 24 March 2022

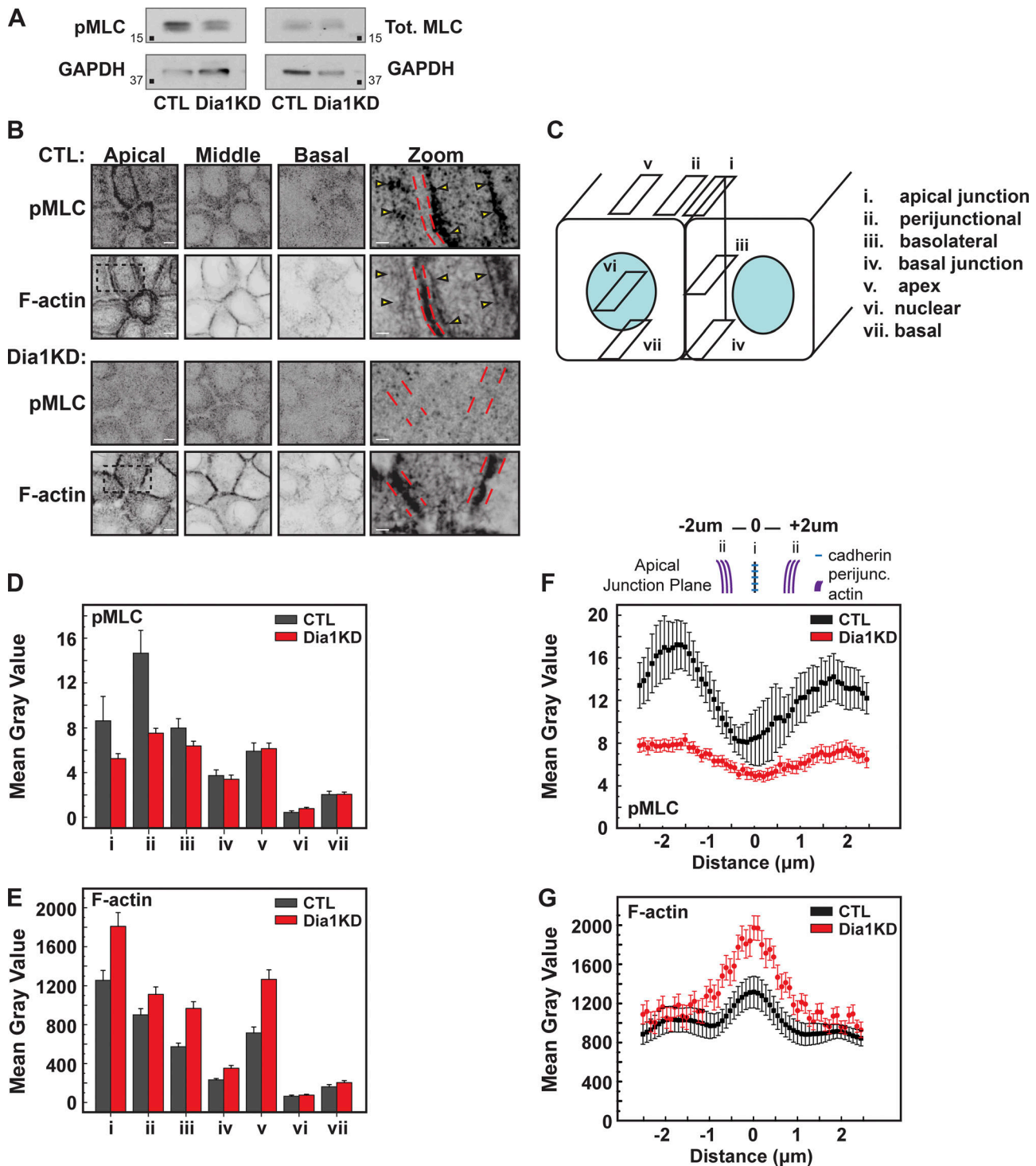


Figure S13. **Dia1 supports perijunctional, myosin-bearing stress fibers during apical junction development.** (A) Western blot of phospho-myosin(s19) light chain and total myosin light chain from CTL and Dia1KD lysates harvested 4 h post-plating. Black squares = molecular weight markers at indicated weight (in kilodaltons). (B) Immunostaining for F-actin and pMLC at the indicated planes, 4 h post-plating. Scale bars = 5 μm (main panels) and 2 μm (zoom panels). (C) Diagram of regions measured in subsequent panels. (D and E) Mean gray values obtained for F-actin and pMLC in the regions depicted in B (n = 15 cells, ±SEM). (F and G) Line scans across intercellular adhesions at the most apical plane of junctions (n = 15 junctions per condition). Data points represent the mean value of these scans at the indicated position ±SEM. Background signals from the underlying collagen were subtracted from fluorescence values prior to graphing.

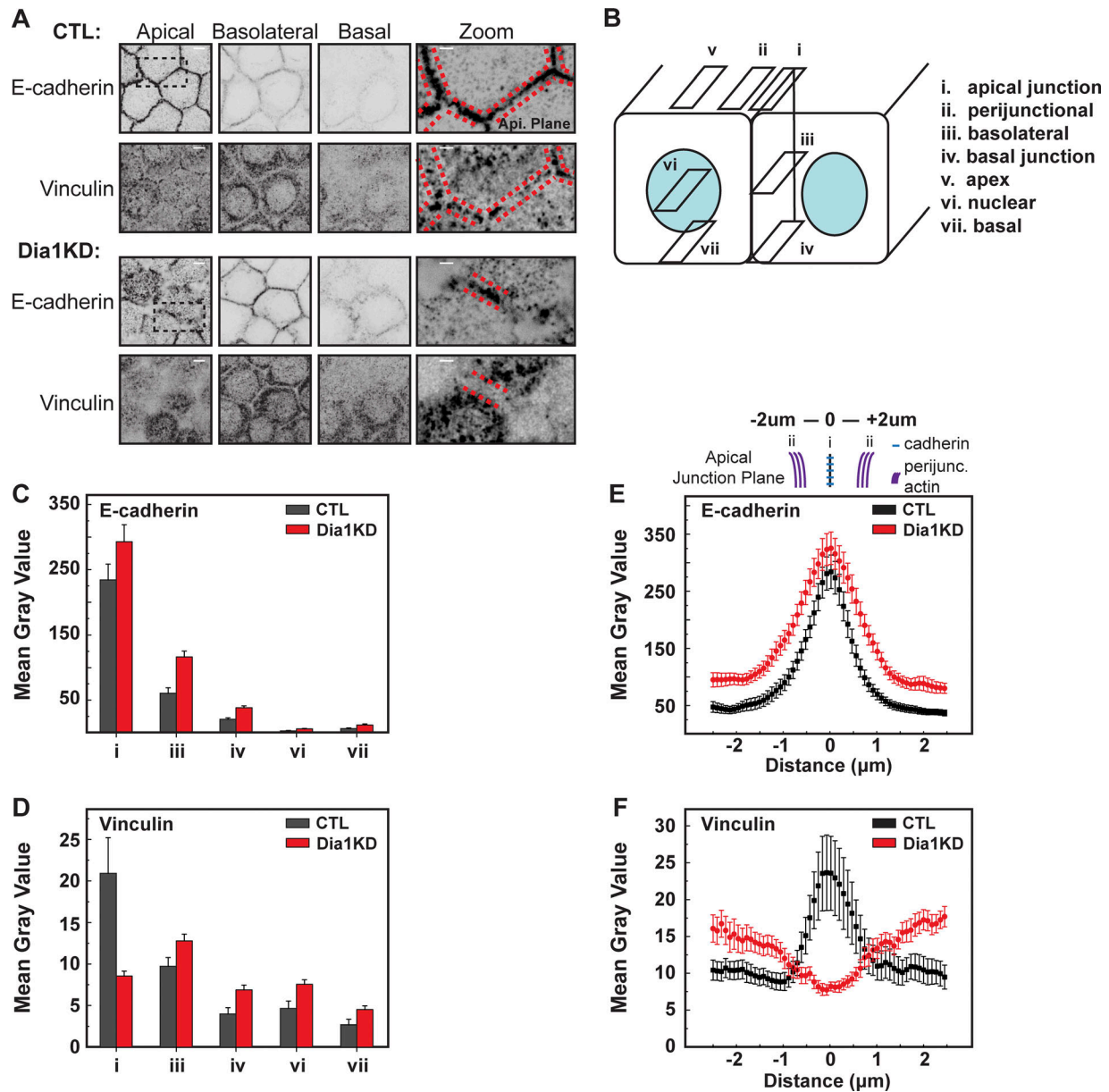


Figure S14. **Dia1 enables maturation of E-cadherin based adhesions at the apical junction.** (A) E-cadherin and vinculin immunostaining at the indicated planes of CTL and Dia1KD cells 4 h after plating. Zoomed in regions are marked by the black dashed box. Red dashed lines enclose E-cadherin based junctions and are overlaid upon the vinculin stain for spatial reference. Scale bars = 5 μm (main panels) and 2 μm (zoom panels). (B) Diagram of regions measured in subsequent panels. (C and D) Mean gray values obtained for E-cadherin and vinculin in the regions depicted in B ($n = 15$ cells, \pm SEM). (E and F) Line scans across intercellular adhesions at the most apical plane of junctions marked by E-cadherin ($n = 15$ junctions per condition). Data points represent the mean value of these scans at the indicated position \pm SEM. Background signals from the underlying collagen were subtracted from fluorescence measurements prior to graphing. For vinculin images, a 1-pixel gaussian blur was applied to reduce noise. Filtered images were not used for quantitation.

Provided online are Table S1, Table S2, Table S3, Table S4, and Table S5. Table S1 lists gene ontology categories upregulated in response to Dia1-rescue derived from RNA-seq data. Table S2 lists vertical positioning of Dia1KD-Scarlet cells with respect to CTL-H2B cells on the boundaries of CTL-H2B cell clusters. Table S3 lists the position of daughter cells derived from dividing, H2B-labeled cells when juxtaposed to Scarlet-labeled neighbors. Table S4 lists density and mitosis of CTL-H2B and Dia1KD-H2B cultures. Table S5 lists density and evaluation of asymmetric division orientation in CTL-H2B and Dia1KD-H2B cultures.